



<b>Publication Year</b>	2023
<b>Acceptance in OA @INAF</b>	2023-05-18T11:51:32Z
<b>Title</b>	SHERLOC Raman Mineral Class Detections of the Mars 2020 Crater Floor Campaign
<b>Authors</b>	Corpolongo, Andrea; Jakubek, Ryan S.; Abbey, William; Asher, Sanford A.; Baker, Desirée; et al.
<b>DOI</b>	10.1029/2022JE007455
<b>Handle</b>	<a href="http://hdl.handle.net/20.500.12386/34157">http://hdl.handle.net/20.500.12386/34157</a>
<b>Journal</b>	JOURNAL OF GEOPHYSICAL RESEARCH (PLANETS)

# SHERLOC Raman Mineral Class Detections of the Mars 2020 Crater Floor Campaign

Andrea Corpolongo<sup>1\*</sup>, Ryan S. Jakubek<sup>2</sup> (remaining contributors in alphabetical order) William Abbey<sup>3</sup>, Sanford A. Asher<sup>4</sup>, Desirée Baker<sup>1</sup>, Luther W. Beegle<sup>5</sup>, Eve L. Berger<sup>6</sup>, Rohit Bhartia<sup>7</sup>, Adrian J. Brown<sup>3</sup>, Aaron S. Burton<sup>8</sup>, Sergei V. Bykov<sup>4</sup>, Emily Cardarelli<sup>3</sup>, Edward A. Cloutis<sup>9</sup>, Pamela Conrad<sup>10</sup>, Andrew D. Czaja<sup>1</sup>, Lauren DeFlores<sup>3</sup>, David Flannery<sup>11</sup>, Teresa Fornaro<sup>12</sup>, Marc Fries<sup>8</sup>, Nikole C. Haney<sup>2</sup>, Keyron Hickman-Lewis<sup>13,14</sup>, Linda Kah<sup>15</sup>, Carina Lee<sup>16</sup>, Francis M. McCubbin<sup>8</sup>, Michelle Minitti<sup>17</sup>, Richard V. Morris<sup>8</sup>, Joseph Razzell Hollis<sup>3</sup>, Ryan Roppel<sup>4</sup>, Eva L. Scheller<sup>18</sup>, Sunanda Sharma<sup>3</sup>, Svetlana Shkolyar<sup>19,20,21</sup>, Sandra Siljeström<sup>22</sup>, Kim Steadman<sup>3</sup>, Andrew Steele<sup>10</sup>, Kyle Uckert<sup>3</sup>, Brittan V. Wogslund<sup>15</sup>, Anastasia Yanchilina<sup>23</sup>

<sup>1</sup>Department of Geology, University of Cincinnati, Cincinnati, OH, USA

<sup>2</sup>Jacobs, NASA Johnson Space Center, Houston, TX 77058, USA

<sup>3</sup>Jet Propulsion Laboratory, California Institution of Technology, Pasadena, CA, USA

<sup>4</sup>Department of Chemistry, University of Pittsburgh, Pittsburgh, PA, USA

<sup>5</sup>Formerly at Jet Propulsion Laboratory, California Institution of Technology, Pasadena, CA, USA

<sup>6</sup>Texas State University - Jacobs JETS - NASA Johnson Space Center

<sup>7</sup>Photon Systems Incorporated, Covina, CA, USA

<sup>8</sup>NASA Johnson Space Center, Houston, TX 77058, USA

<sup>9</sup>Department of Geography, University of Winnipeg, Winnipeg, Manitoba, Canada

<sup>10</sup>Carnegie Institute of Washington, Washington, DC, USA

<sup>11</sup>Queensland University of Technology, Brisbane, Queensland, Australia

<sup>12</sup>INAF-Astrophysical Observatory of Arcetri, Florence, Italy

<sup>13</sup>The Natural History Museum, London, UK

<sup>14</sup>Dipartimento BiGeA, Università di Bologna, Bologna, Italy

<sup>15</sup>Department of Earth and Planetary Sciences, University of Tennessee, Knoxville, TN, USA

<sup>16</sup>Lunar & Planetary Institute, Universities Space Research Association, Houston, TX, USA

<sup>17</sup>Framework, Silver Spring, MD, USA

<sup>18</sup>California Institute of Technology, Pasadena, CA, USA

<sup>19</sup>USRA, Columbia, MD, USA

<sup>20</sup>NASA Goddard Space Flight Center, Greenbelt, MD, USA

<sup>21</sup>Blue Marble Space Institute of Science, Seattle, WA, USA

<sup>22</sup>RISE Research Institutes of Sweden, Stockholm, Sweden

<sup>23</sup>Impossible Sensing Incorporated, St. Louis, MO, USA

\*Corresponding author: Andrea Corpolongo ([corpola@mail.uc.edu](mailto:corpola@mail.uc.edu))

This article has been accepted for publication and undergone full peer review but has not been through the copyediting, typesetting, pagination and proofreading process, which may lead to differences between this version and the [Version of Record](#). Please cite this article as [doi: 10.1029/2022JE007455](https://doi.org/10.1029/2022JE007455).

This article is protected by copyright. All rights reserved.

**Key Points:**

- The floor of Jezero Crater hosts distinct igneous units with differing aqueous alteration histories.
- SHERLOC Raman mineral class detections indicate that the Jezero crater floor was once a habitable environment.
- Some Crater Floor Campaign samples may contain salts known to preserve biosignatures in terrestrial analogue environments.

## Abstract

The goals of NASA's Mars 2020 mission include searching for evidence of ancient life on Mars, studying the geology of Jezero crater, understanding Mars' current and past climate, and preparing for human exploration of Mars. During the mission's first science campaign, the Perseverance rover's SHERLOC deep UV Raman and fluorescence instrument collected microscale, two-dimensional Raman and fluorescence images on ten natural (unabraded) and abraded targets on two different Jezero crater floor units: Séítah and Máaz. We report SHERLOC Raman measurements collected during the Crater Floor Campaign and discuss their implications regarding the origin and history of Séítah and Máaz. The data support the conclusion that Séítah and Máaz are mineralogically distinct igneous units with complex aqueous alteration histories and suggest that the Jezero crater floor once hosted an environment capable of supporting microbial life and preserving evidence of that life, if it existed.

## Plain Language Summary

The goals of NASA's Mars 2020 mission include searching for evidence of ancient life on Mars, studying the geology of Jezero crater, understanding Mars' current and past climate, and preparing for human exploration of Mars. During the mission's first science campaign, SHERLOC (Scanning Habitable Environments with Raman & Luminescence for Organics and Chemicals), one of Perseverance rover's spectroscopic instruments, collected microscale, two-dimensional images that display mineral and organic molecule detections on ten natural (unabraded) and abraded targets on two different Jezero crater floor geological units: Séítah and Máaz. We report SHERLOC mineral detections made during the Crater Floor Campaign and discuss their implications regarding the origin and history of Séítah and Máaz. The mineral detections support the conclusion that Séítah and Máaz are igneous units with different mineral compositions and distinct histories of alteration by fluids. The detections further suggest that the Jezero crater floor was once home to an environment capable of supporting microbial life and preserving evidence of that life, if it ever existed.

## 1 Introduction

On 18th February 2021, NASA's Mars 2020 mission Perseverance rover began exploring Jezero crater with the primary goal of searching for evidence of ancient life on Mars. Other goals include studying the geology of the region, understanding Mars' current and past climate, and preparing for human exploration (Farley et al., 2020). These goals are being addressed through *in situ* analyses by the rover's instruments and collection of a suite of compelling samples to be returned to Earth by future Mars Sample Return (MSR) missions.

The first campaign of the Mars 2020 mission was an exploration of the floor of Jezero crater (Sun et al., 2022; Fig. 1). During this campaign, the rover investigated two major units, Séítah and Máaz, on the floor of Jezero crater that had been identified from orbital data before surface operations commenced (Stack et al., 2020). (Note that special characters and accents in target, rock, and unit names are omitted in many Mars 2020 documents because they cannot be included in code used to communicate with Perseverance. As a result, alternate spellings, such as , Seitah, Maaz, and Chal, are often used for features with accents or special characters in their names.) The older unit, Séítah, previously referred to as the Crater Floor Fractured 1 (CF-F-1) Unit, is light-toned, ridged, and fractured. Séítah is overlain by Máaz, previously referred to as the Crater Floor Fractured Rough (CF-Fr) Unit, which is light-toned and polygonally fractured.

Results from the Perseverance payload during the Crater Floor Campaign indicate that both Máaz and Séítah are igneous in origin (Horgan et al., 2022). Máaz is characterized by the presence of abundant pyroxene (Schmidt et al., 2022; Udry et al., 2022), while Séítah is an olivine cumulate (Brown et al., 2022; Farley et al., 2022; Liu et al., 2022; Nuñez et al., 2022; Wiens et al., 2022). The transition between the Séítah and Máaz units is highlighted in cyan in Figure 1. The contact between the two units is obscured by regolith and not observable, however Séítah and Máaz vary in elevation by approximately 10 meters along Artuby ridge (Fig. 1), a resistant feature along the southern margin of the portion of the Séítah unit that Perseverance explored (Sun et al., 2022).

The Crater Floor Campaign addressed several objectives of the Mars 2020 mission by contributing to a scientific understanding of the geology of Jezero crater, seeking rocks with a high probability of preserving ancient biosignatures and looking for potential biosignatures within rocks of the Séítah and Máaz units, and documenting the geological context of the first set of samples collected for possible future return to Earth. This paper reports spectral maps collected by SHERLOC (Scanning Habitable Environments with Raman and Luminescence for Organics and Chemicals), an arm mounted deep UV (DUV) Raman spectrometer (Bhartia et al., 2021). The maps are paired with high resolution (10.1  $\mu\text{m}/\text{pixel}$ ) grayscale images collected by the co-boresighted Autofocus Context Imager (ACI), enabling mapping of the location where each Raman spectrum was collected on the target surface. In addition, the Wide Angle Topographic Sensor for Operations and eNgeering camera (WATSON) provides macro-scale, color images of the Raman scan targets. Combining the image color of WATSON images with the high resolution of the ACI images produces colorized ACI images that allow for the identification of individual mineral grains and the detection of associations between minerals and any detected organic matter. These capabilities make SHERLOC and WATSON of central importance to achieving the geological and astrobiological objectives of the Mars 2020 mission.

**Figure 1.** Map of the Crater Floor Campaign traverse (central image and insets, based on HiRISE imagery) and natural and abraded targets analyzed by proximity science, including SHERLOC and WATSON, through sol 370 (smaller images around the periphery, imaged by the MastCam-Z instrument on the Perseverance rover). The white path on the map shows Perseverance's traverse. The cyan line marks the approximate contact between the Séítah formation below and the Máaz formation above. The red bracket indicates Artuby Ridge. Targets analyzed are indicated along the route. The yellow circles on most targets indicate the location of abrasion patches (see subsequent figures). Those without yellow circles were not abraded.

## 2 Methods

SHERLOC is a deep UV (DUV) Raman and fluorescence spectrometer designed to detect, characterize, and spatially resolve organics and minerals on the Martian surface (Bhartia et al., 2021). A 248.6 nm DUV laser is used for excitation and takes advantage of increased scattering Raman cross section from Rayleigh Law and resonance enhancement, allowing for the detection of small quantities of organics and minerals. Many molecules, when excited, fluoresce at wavelengths above  $\sim 270$  nm, at intensities many orders of magnitude greater than the intensities of typical Raman peaks, making it difficult to impossible to detect any Raman scattering that might coincide with such strong fluorescence bands. Unlike longer wavelength lasers (near-UV, visible, or near IR) the DUV Raman window is energetically separated from the fluorescence window, allowing for Raman and fluorescence spectra to be obtained in non-overlapping spectral regions (Tarcea et al., 2007; Bhartia et al., 2012; Eshelman et al., 2014; Montagnac et al., 2021). The depth of field of the SHERLOC instrument is  $\pm 500$   $\mu\text{m}$  to

accommodate the surface roughness of the abraded patch however, it is expected that the Raman response is coming from a 100–200  $\mu\text{m}$  depth of penetration (Bhartia et al., 2021, Carrier et al., 2019). The DUV laser-injection filter optical coating attenuates  $< 800\text{ cm}^{-1}$ , limiting detection of primary Raman bands of many silicates and oxides. In addition, DUV absorbing minerals (i.e., some Fe containing minerals) can attenuate the depth of penetration into a material and reduce signal to noise ratios (SNR) (Morris et al., 2022; Razzell Hollis et al., 2021a).

SHERLOC is an arm-mounted instrument, which allows it to be moved into proximity of an analysis target. With no change in arm position, an internal scanning mirror rasters the deep UV laser beam across the sample surface. With a maximum area of  $7 \times 7\text{ mm}$ , Raman/fluorescence spectra are acquired at discrete points with a beam diameter of  $\sim 100\text{ }\mu\text{m}$  (Bhartia et al., 2021). Prior to each spectrum scan, the Autofocus Context Imager (ACI) is used to acquire  $10.1\text{ }\mu\text{m}/\text{pixel}$  resolution grayscale images of the target surface. This provides context for the spectral maps and is used to focus the spectrometer/laser. Color images acquired by WATSON have a spatial resolution ranging from 16 to  $150\text{ }\mu\text{m}/\text{pixel}$  and are used for targeting SHERLOC observations and textural analysis (Bhartia et al., 2021; Edgett et al., 2012; Wogoland et al., this issue). SHERLOC is designed to simultaneously collect Raman and fluorescence data on the same CCD with a single readout. To reduce noise, the CCD readout is binned into 3 regions, a Raman region  $\sim 800$  to  $4000\text{ cm}^{-1}$  (250 to 273 nm) and two fluorescence regions (274 to 337 and 338 to  $\sim 370\text{ nm}$ ). Each region has a separate wavenumber calibration, previously discussed in detail (Uckert et al., 2021).

## 2.1 Scan Procedures

In this paper, we use the following nomenclature to describe SHERLOC Raman measurements (Fig. S1). A “target” refers to the specific rock or abraded patch on which data were collected, such as “Nataani” or “Guillaumes,” while a “scan” refers to a specific Raman hyperspectral map that was collected on a target. Each Raman scan is named using the nomenclature “#0001\_name\_#2\_#3”, wherein #0001 denotes the sol on which the scan was performed, name refers to the target and describes the parameters of the scan, #2 is the laser pulses per each point spectrum within a scan, and #3 is the scan number used to differentiate between multiple scans of the same parameter made on the same sol. Each individual spectrum within a scan is referred to as a “point,” and each point within a scan is assigned a number according to the order it occurred in the scan. The first Raman spectra collected within a scan falls at the upper left corner of the hyperspectral map. Collection continues in a serpentine pattern, such that the final spectra in a 100 point scan falls at the lower left corner of the map. High Dynamic Range (HDR) scans consist of 100 points with  $780\text{ }\mu\text{m}$  spacing for an image size of  $7 \times 7\text{ mm}$ . Detail scans consist of 100 points with  $100\text{ }\mu\text{m}$  spacing for an image size of  $1 \times 1\text{ mm}$ . Survey scans consist of 1296 points with fixed spacing between them (50, 144, or  $200\text{ }\mu\text{m}$ , depending on the scan template) and 10 or 15 pulses per point. For example, the scan name “0083\_Nataani HDR\_50\_1” describes the first HDR scan performed on Nataani using 50 pulses per point on sol 83 of the Mars 2020 mission.

For each scan SHERLOC performs, single spectra are obtained by first collecting a dark spectrum with no incident laser light and then collecting the active spectrum with the laser firing. The dark scan is then subtracted from the active spectrum to produce the reported Raman spectrum. SHERLOC spectra have a  $\sim 10\text{ cm}^{-1}/\text{pixel}$  resolution with a Raman spectral range of  $\sim 800$ – $4000\text{ cm}^{-1}$ . The potential to observe Raman bands in the spectral range below  $800\text{ cm}^{-1}$  is limited because SHERLOC’s laser-injection filter has reduced transmission in this region and the

252.9 nm laser plasma line is observed at  $\sim 650\text{ cm}^{-1}$ . However, very strong bands below  $800\text{ cm}^{-1}$  can be observed (Bhartia et al., 2021; Uckert et al., 2021; Razzell Hollis et al., 2021a).

We performed scans on both natural and abraded targets. Targets were abraded using Perseverance's Rock Abrasion Tool (RAT), which is  $\sim 45\text{ mm}$  in diameter and capable of creating smooth-bottomed abraded patches up to  $\sim 1\text{ cm}$  deep. After abrasion, abraded patches are cleaned of dust and cuttings by the gaseous dust removal tool (gDRT), which blasts the abraded target with a high-velocity jet of nitrogen gas (Farley et al., 2020; Moeller et al., 2021). The targets described below as abraded targets were abraded and cleaned as described prior to scanning. Any targets described below as natural targets were neither abraded nor cleaned with the gDRT prior to scanning.

## 2.2 Data Analysis Procedures

We examined each individual Raman spectrum in each scan. We considered any band with a FWHM of  $30\text{ cm}^{-1}$  ( $\sim 3$  pixels) or more a potential Raman signal. We assigned each single spectrum containing observable Raman signals to its respective mineral class via comparison to standard spectra obtained through laboratory measurements with the SHERLOC Brassboard instrument, an analogue DUV Raman and fluorescence instrument housed at the NASA Jet Propulsion Laboratory (described in detail by Razzell-Hollis et al., 2021a,b) and ACRONM (Analogue Complementary Raman for Operations on Mars) (see section S4.1 for a discussion of SHERLOC analogue instruments). All peak centers were determined with a Gaussian fit function, through the open-source peak fitting software Fityk (version 1.3.1; Wojdyr, 2010).

In section 3.0, we display the SHERLOC Raman data through Raman spectral assignments overlain on each scan's associated ACI image. These spectral assignment maps are accompanied by colorized ACI images overlaid with white rings that indicate the location of each point in the scan. The spectral positioning calculations were validated from images of ACI calibration measurements where dust mobilization could be observed. Spectral map/ACI overlays are accurate to within  $\sim 44\text{ }\mu\text{m}$  near the center of maps, and within  $115\text{ }\mu\text{m}$  at the  $7\times 7\text{ mm}$  map corners in the HDR overlays. The points at the start of each scan (scans start at the upper left corner) have less location uncertainty than points at the end of the map scan because of robotic arm drift, which can add up to  $\sim 30\text{ }\mu\text{m}$  of uncertainty. Each laser shot hits the scanned surface as an annulus  $\sim 100\text{ }\mu\text{m}$  in diameter. The white rings overlying the colorized ACI images are  $\sim 200\text{ }\mu\text{m}$  in diameter so that the location being analyzed is visible.

We used Bayer-encoded 8-bit WATSON color and grayscale ACI image products for this study to most closely represent the raw data from the image detector. To generate secondary image products, we performed further processing on both WATSON and ACI products using a custom Python script to register multiple images for a single target to create an overlay. ACI companded image products and WATSON companded or companded z-stack range images ( $\sim 4\text{ cm}$  to  $10\text{ cm}$  standoff) images were used in all cases. "Colorized" ACI images used for correlating spectral, color, and textural information were generated as previously described (Scheller et al., 2022).

## 2.3 Spectra Signal-to-Noise Analysis

In order to quantitatively assign confidence to SHERLOC mineral detections, we developed a statistical procedure involving comparing apparent signal intensities to a calculated median root-mean-squared-deviation (RMSD) of the noise for each scan. We first calculated the noise RMSD in the  $2500\text{--}3000\text{ cm}^{-1}$  region of Raman spectra for every individual spectrum in

each scan. This “silent” region was selected for its lack of signal in any spectrum, excluding cosmic ray artifacts. Then we determined the median of the noise RMSD values for each scan. We used the median to avoid contributions from any RMSD values that were inflated by cosmic rays, background fluorescence, and other spectral effects. The RMSD noise values differed between Raman images but generally occur in the 20-50 count range.

We designated single spectra Raman bands with intensities  $\geq 3X$  the noise RMSD as statistically significant signals. This designation criterion is based on the International Union of Pure and Applied Chemistry’s limit of detection for the probability of a data point being statistically above a normally distributed noise background (McNaught & Wilkinson, 1997). The peak position error for SHERLOC Raman bands with intensities  $\geq 3X$  the noise RMSD is  $\leq \pm 4.0 \text{ cm}^{-1}$ . We used mean spectra to assign detections to mineral classes. By doing so, we obtained spectra with maximum peak intensities  $\geq 10X$  the noise RMSD, which have a peak position error of  $< \pm 1 \text{ cm}^{-1}$ . *Combined with the  $\pm 1.8 \text{ cm}^{-1}$  uncertainty in the wavenumber calibration (Fries et al. 2022), the peak wavenumber error of the most intense peaks in spectra used to assign mineral classes is approximately  $\pm 2-3 \text{ cm}^{-1}$ . However, the error for any specific peak in a single spectrum is dependent on signal-to-noise ratio and can be estimated using the work of Lenz and Ayres 1992 as described in section S1.0 of the supporting information. In the main text, the peak wavenumber values reported are approximate values for a mineral class assignment and are only meant to qualitatively describe the spectra for discussion. As described in the supporting information, most mineral class assignments were assigned based on multiple Raman bands, and for mineral classes where only one band is present (carbonate, pyroxene, and silicate), the bands have distinctive Raman shifts. Thus, the mineral class assignments are not peak wavenumber error limited.*

In the context of this paper, signals with  $\geq 3X$  the noise RMSD are qualitatively observed with high confidence while those  $< 3X$  are observed with less confidence. For these reasons, in the ACI-Raman image overlay figures presented in section 3, we differentiate between Raman signals  $\geq 3X$  and  $< 3X$  the RMSD noise as a first-order indicator of the assignment confidence. To make this distinction, we label assignments made based on Raman signals  $\geq 3X$  the noise with capital letters and those made based on signals  $< 3X$  the noise with lowercase letters. In the text, we describe assignments made based on Raman signals  $\geq 3X$  the noise as definitive and assignments made based on signals  $< 3X$  the noise as probable or possible.

## 2.4 Background Spectral Features

It is important to note several spectral features observed as background in SHERLOC Raman spectra. These features are characterized by Raman scans collected with no target at the laser focus, referred to as the stowed arm scans. We collected HDR\_100, \_250, and \_500 scans with SHERLOC in the stowed position. We detected a weak Raman peak of fused silica that originated from Raman scattering of the instrument optics, seen as broad peaks at  $\sim 480 \text{ cm}^{-1}$  and  $\sim 800 \text{ cm}^{-1}$  (section S2). This background feature is of sufficiently weak intensity that it is observed only in spectra with  $\geq 500$  pulses/point. In addition, the fused silica background is distinct from all Raman signals obtained from sample targets and does not interfere with spectral analysis.

We also observed narrow peaks occurring at specific wavenumbers more frequently than would be expected if they were occurring randomly. These peaks are artifacts of the dark spectrum subtraction process described in section 2.1. Most of the artifact peaks occur at



wavenumbers that are irrelevant to the spectral assignments in this paper. However, we observed narrow peaks at  $970\text{ cm}^{-1}$  and/or  $981\text{ cm}^{-1}$  in  $\sim 20\%$  of the stowed arm spectra, which increases the uncertainty of spectral assignments relying on peaks at or near these wavenumbers. At the time of writing, the SHERLOC team is working to determine the cause and mitigate the influence of these artifacts. See section S3 for a detailed discussion of this topic.

### 3 Results

SHERLOC scanned 10 targets during the Crater Floor Campaign: three from Séítah (all abraded surfaces) and seven from Máaz (three natural and four abraded surfaces) (Fig. 1). SHERLOC successfully performed within operating capabilities on Mars, becoming the first Raman spectrometer to map mineral composition in context on the surface of another planetary body.

In sections 3.1 and 3.2, beginning with the stratigraphically lower Séítah targets and moving upsection to Máaz targets, we report the results of SHERLOC's microscale mineral mapping on the Jezero Crater floor. For each target, we describe textural features of the scanned rock surfaces revealed by WATSON imagery (Wogsland et al., this issue), report mineral detections facilitated by SHERLOC Raman spectroscopy at each target, and highlight associations between textural features and mineral detections.

Mineral assignments reported below are to mineral class only, not to mineral species, with the exception of sodium perchlorate assignments reported in section 3.2.1. Assignments include undefined silicate (labeled silicate throughout the text), carbonate, olivine, perchlorate/phosphate, perchlorate, sodium perchlorate, pyroxene, and sulfate. Class assignments were made by comparing fitted mean or individual SHERLOC spectra (as specified in the individual reports below) to standard spectra collected with the DUV SHERLOC analogue instruments Brassboard and ACRONM, as shown in figures 2 through 8.

Spectra assigned to undefined silicate feature a broad band centered at  $\sim 1050\text{ cm}^{-1}$  that is similar to broad bands between  $900$  to  $1200\text{ cm}^{-1}$  observed in some silicate spectra collected on ACRONM. The bands are qualitatively similar to ACRONM spectra of plagioclase feldspar (Figs. 2, 3, 6, 7, 8). However, the identifying Raman peaks of feldspars (and many other silicates) occur below  $800\text{ cm}^{-1}$ , in the spectral range that is obscured by SHERLOC's laser-injection filter and laser plasma line. Some of the broad bands centered at  $\sim 1050\text{ cm}^{-1}$  could represent detections of amorphous silica, as amorphous silica would yield spectra with a similar feature (Fu et al., 2017). However, the broad nature of these bands is also similar to broad bands centered between  $1000$  and  $1020\text{ cm}^{-1}$  in augite, labradorite, and bytownite spectra collected on Brassboard (Razzell-Hollis et al., 2021a), which further indicates that SHERLOC scans of crystalline silicates may yield broad spectral features. As a result, we cannot make more specific mineral assignments of spectra featuring broad bands centered at  $\sim 1050\text{ cm}^{-1}$  at this time, as they may represent detections of crystalline or amorphous mineral phases. The SHERLOC team is actively working to determine exactly how the laser injection filter effects peak intensity and placement in the spectral range below  $800\text{ cm}^{-1}$ . This work will be reported in a future publication. Unlike other silicates, the Raman spectra of olivine and pyroxene have identifying peaks above  $800\text{ cm}^{-1}$ , allowing us to assign SHERLOC spectra to these mineral classes.

The dominant peaks in pyroxene and sulfate Raman spectra can fall within the same spectral range, of  $\sim 970\text{ cm}^{-1}$  to  $1050\text{ cm}^{-1}$  (e.g., Razzell Hollis et al., 2021a). We differentiated between these assignments based on the presence of characteristic secondary peaks and hydration features in sulfate spectra, and by confirming pyroxene assignments with data

collected by PIXL, Perseverance's micro-X-Ray fluorescence spectrometer, when possible. The dominant peaks of perchlorate and phosphate fall in a partially overlapping spectral range, between  $\sim 950\text{ cm}^{-1}$  and  $970\text{ cm}^{-1}$ . Where we observed peaks in this range, we distinguished between phosphate and perchlorate based on the presence of secondary perchlorate peaks. Where we observed peaks between  $\sim 950\text{ cm}^{-1}$  and  $970\text{ cm}^{-1}$  with no secondary peaks, we assigned spectra to perchlorate/phosphate. Criteria for all mineral assignments reported below are discussed in greater detail in the supporting information (section S4).

### 3.1 Séítah Targets

#### 3.1.1 Dourbes

The Dourbes abrasion, which was approximately 7 mm deep, was made on sol 251 on Brac, an outcrop of the Bastide member of the Séítah formation that featured centimeter to decimeter scale layering (Fig. 1). The pre-abrasion surface of Brac was fluted from apparent wind abrasion and dust coated (Fig. S2A). The lowest relief areas of the surface of Brac were filled with coarse regolith and fine-grained gravel. Two core samples retrieved from Brac, Salette and Coulettes, are associated with the Dourbes abrasion. The abraded surface of Dourbes features  $\sim 1\text{--}3\text{ mm}$  angular light gray-to-green and dark brown-to-black mineral grains (Figs. 2A-C). The gray-to-black grains are highly reflective. These grains are frequently rimmed by a light tan material and a reddish-brown material occurs in the spaces between them. The surface of Dourbes has no pitting or staining.

SHERLOC scans of Dourbes include 0257\_Dourbes Survey\_15\_1, 0257\_Dourbes HDR\_500\_1, 0269\_Dourbes Survey\_15\_1, 0269\_Dourbes Detail\_500\_1, 0269\_Dourbes Detail\_500\_2, and 0269\_Dourbes Detail\_500\_3 (Fig. 2). The individual spectra from the Dourbes Survey scans contain no discernible peaks. The mean spectra of each of these scans has a very weak possible silicate band (see section S4.2), a weak possible O-H stretching band, and the background fused silica spectra discussed in section 2.4 (Fig. S1b). The remaining scans contain spectra consistent with olivine, carbonate, pyroxene, sulfate, and perchlorate or phosphate in addition to silicate (Figs. 2B-D).

Olivine was the most common detection in 0257\_Dourbes HDR\_500\_1 (Fig. 2B). Thirty-eight percent of the points in this scan were definitively assigned to olivine and a further 8% were assigned as probable olivine. The dominant peak in the mean spectrum of all points in 0257\_Dourbes HDR\_500\_1 definitively assigned to olivine is centered at  $827\text{ cm}^{-1}$  (Fig. 2D). The olivine standard spectrum in figure 3D was collected with Brassboard from a natural forsterite sample (WARDS) and exhibits a primary peak centered at  $844\text{ cm}^{-1}$ . Neither SHERLOC nor Brassboard has the spectral resolution required to resolve the doublet at  $\sim 820\text{ cm}^{-1}$  and  $\sim 850\text{ cm}^{-1}$  that is typically observed in olivines and can be used to determine olivine composition (Chopelas, 1991; Kuebler et al., 2006; Razzell Hollis et al., 2021a). Correlating SHERLOC's unresolved olivine doublets to olivine Fo content is beyond the scope of this paper, as changes in the unresolved band position and width are controlled by the relative positions and intensities of the individual  $\sim 820$  and  $\sim 850\text{ cm}^{-1}$  bands (see section S4.3).

Carbonate and pyroxene were also prominent detections in this scan, with 5% of the points definitively assigned to carbonate, 6% assigned probable carbonate, 4% definitively assigned to pyroxene, and 5% assigned probable pyroxene. In addition, one point was definitively assigned to silicate and two were assigned as probable silicates. One point in this scan was definitively assigned to sulfate. The mean spectrum of all points in 0257\_Dourbes

HDR 500\_1 definitively assigned to pyroxene is centered at  $993\text{ cm}^{-1}$ , which is consistent with the augite spectrum collected by Brassboard (Fig. 2D). The comparison to a standard augite spectrum is not a formal mineral species assignment, which will require a detailed investigation that is beyond the scope of this paper. This peak could also be consistent with hydrated sulfate species. We determined that the Dourbes points assigned to pyroxene are unlikely to be sulfate because they lack detectable hydration features and because PIXL, Perseverance's micro-X-Ray fluorescence spectrometer that provides spatially resolved elemental abundances, detected silicon, magnesium, and aluminum, but no sulfur, in the region of these detections, which is consistent with the presence of pyroxene (Razzell Hollis et al., 2022).

The three Dourbes Detail scans yielded sulfate, carbonate, olivine, silicate, perchlorate, and phosphate or perchlorate detections. Scan 0269\_Dourbes Detail\_500\_1 is dominated by sulfate detections surrounded by carbonate detections, much like the larger carbonate rimmed sulfate in Quartier (Figs. 4C; see section 3.1.3). The dominant peak in the mean spectrum of all points in 0269\_Dourbes Detail 500\_1 assigned to sulfate only is centered at  $1022\text{ cm}^{-1}$ , represented by the vertical solid red line in figure 2D. This mean spectrum also has weak secondary peaks at  $1141\text{ cm}^{-1}$  and  $1220\text{ cm}^{-1}$ , represented by the dotted and dashed vertical red lines in figure 2D, and an OH stretching mode band (Fig. S10b). The primary peak in the Dourbes sulfate spectrum agrees closely with the primary peak of a synthetic magnesium sulfate (Macron Chemicals) spectrum collected on Brassboard, which is centered at  $1019\text{ cm}^{-1}$  (Fig. 4D). The secondary peaks of the Brassboard magnesium sulfate spectrum are at  $1150\text{ cm}^{-1}$  and  $1274\text{ cm}^{-1}$ . While these peaks do not correspond directly to the secondary peaks in the Dourbes sulfate spectrum, the secondary peaks of magnesium sulfate are reported to vary between  $\sim 1060\text{ cm}^{-1}$  and  $\sim 1260\text{ cm}^{-1}$ , depending on the hydration state of the mineral (Wang et al., 2006). The sulfate detections are concentrated on a sub-millimeter light brown to white grain (Figs. 2C and 9B).

The single definitive perchlorate or chlorate detection in Dourbes is at point 11 of scan 0269\_Dourbes Detail\_500\_1 (Figs. 2C and S12). This detection co-occurs with a definitive sulfate detection and falls at the edge of the light brown to white sulfate grain, adjacent to carbonate detections. We made this perchlorate assignment based on the presence of a peak at  $932\text{ cm}^{-1}$ , which is consistent with the primary peak of several different perchlorate and chlorate species (see section S4.8).

The dominant peak in the mean spectrum of all points in 0269\_Dourbes Detail 500\_1 assigned to carbonate is centered at  $1083\text{ cm}^{-1}$ , represented by the vertical cyan line in figure 2D. This peak corresponds closely to the  $1084\text{ cm}^{-1}$  peak in the Brassboard terrestrial calcite standard spectrum (WARDS #49–5860) (Fig. 2). The similarity between these spectra could suggest that the Dourbes carbonates are primarily calcite (see section S4.4). However, this comparison is made with a mean spectrum of all carbonate points in the scan, so it is likely that carbonates with different cations are contributing to the average peak position. Furthermore, minerals containing iron cations can absorb DUV laser radiation (Morris et al., 2022; Razzell Hollis et al., 2021a and b). This effect would have interfered with data acquisition if any of the detected carbonates contained iron. Therefore, we cannot assign SHERLOC carbonate detections to specific mineral species. The carbonate detections correspond to reddish-brown grains, primarily at the edge of the sulfate grain.

Scan 0269\_Dourbes Detail\_500\_2 is the only SHERLOC scan of the Séítah formation in which the most common mineral detection is silicate. It also features olivine, carbonate, and perchlorate or phosphate detections. The band in the mean spectrum of all points in 0269\_Dourbes Detail 500\_1 assigned to silicate is centered at  $1065\text{ cm}^{-1}$  and has a FWHM of

180  $\text{cm}^{-1}$  (Fig. 2D). This mean spectrum is similar to a labradorite spectrum standard collected with ACRONM. However, this similarity is not sufficient to assign the Dourbes silicate spectra to labradorite (Fig. 2D). The silicate detections correspond with micron scale light gray-to-blue mineral grains. See section S4.2 for additional details regarding silicate detections during the Crater Floor Campaign.

The perchlorate or phosphate peak in the mean spectrum of the three perchlorate or phosphate spectra in 0269\_Dourbes Detail\_500\_2 is centered at  $\sim 958 \text{ cm}^{-1}$  (Fig. 4D). This falls between the dominant peak of a sodium perchlorate standard spectrum (collected with Brassboard from a sample of synthetic sodium perchlorate hydrate powder, Sigma Aldrich 310514) and that of a series of eleven natural and synthetic phosphate standards (collected with ACRONM and includes the minerals fluorapatite, hydroxylapatite, chlorapatite, whitlockite, and merrillite), which makes a confident mineral assignment difficult (Fig. 2D). We observed no hydration features in the Dourbes perchlorate/phosphate spectra. Assignment of SHERLOC Raman peaks between  $\sim 950 \text{ cm}^{-1}$  and  $990 \text{ cm}^{-1}$  is further complicated by the presence of relatively frequent artifacts at  $970 \text{ cm}^{-1}$  and  $981 \text{ cm}^{-1}$  in SHERLOC scans (see sections 2.4 and S3). These artifacts are easily identified when they occur in the absence of Raman signal. However, if they occur in a spectrum with a Raman signal between  $\sim 950 \text{ cm}^{-1}$  and  $990 \text{ cm}^{-1}$ , they may artificially shift the center of the Raman peak.

Scan 0269\_Dourbes Detail\_500\_3 detected olivine, carbonate, and, at a single point that overlaps with 0269\_Dourbes Detail\_500\_1, sulfate. The dominant peak in the mean spectrum of all points in 0269\_Dourbes Detail\_500\_3 assigned to olivine only is centered at  $834 \text{ cm}^{-1}$ . The olivine detections in the lower left corner of this scan correspond with a relatively large, reflective, dark brown-to-black euhedral mineral crystal and are not directly associated with carbonate detections (Fig. 2C). Olivine detections in the upper left corner of this scan fall on a smaller, subhedral, black mineral crystal and are adjacent to carbonate detections that fall on a light reddish-brown grain (Fig. 2C).

**Figure 2.** SHERLOC Raman mineral identifications from Dourbes. A) The abrasion patch imaged by WATSON (image ID SI1\_0257\_0689775622\_738FDR\_N0080000SRLC00006\_000095J01). Yellow boxes indicate the location of the scans performed. B) Colorized (left) and grayscale (right) ACI images (image ID SC3\_0257\_0689786306\_125FDR\_N0080000SRLC11421\_0000LMJ01) of the region of the abrasion patch bounded by the larger yellow box in panel A. The white circles in panel B indicate the locations of SHERLOC analysis spots. Mineral identifications are indicated in the right panel. C) Colorized (left) and grayscale (right) ACI images (image ID SC3\_0269\_0690851147\_347FDR\_N0080000SRLC11373\_0000LMJ02) of the region of the abrasion patch bounded by the smaller yellow boxes in panel A. The white and yellow circles in the upper right subpanel of panel C indicate the locations of SHERLOC analysis spots for three  $1 \text{ mm}^2$  Detail scans. The lower three subpanels show mineral identifications for these three Detail scans. D) Representative Raman spectra of minerals detected with high confidence from the abrasion patch and spectra of mineral standards collected on the SHERLOC Brassboard instrument at JPL and the ACRONM instrument at JSC. Vertical lines indicate peak centers. Spectra are offset along the y-axis for clarity.

### 3.1.2 Garde

The abrasion patch Garde, which was approximately 11 mm deep, was made on sol 206 on the upper surface of a platy layered outcrop of the Bastide member of the Séítah formation, called Bastide (Fig. 1). The Bastide member is characterized by pronounced tabular layering, with most layers 1–3 cm thick and some 10–40 cm thick layers (Farley et al., 2022). The pre-abrasion surface of Garde was dust-coated, with occasional 2–3 mm, angular, elongate, gray-to-green mineral grains visible through the dust (Fig. S2B). Similar grains were recognized in

SuperCam RMI images of relatively fresh outcrop surfaces and identified as olivine (Farley et al., 2022). The surface also exhibited infrequent millimeter scale pitting. No coring was attempted at this outcrop and no core samples are associated with the Garde abrasion.

The abraded surface of Garde has a relatively homogeneous texture (Fig. 3A). It features reflective, light-to-dark gray-green, angular, millimeter-scale mineral grains in a fine-grained light-toned matrix and reflective, dark gray-to-black angular mineral grains that range in size from approximately 1–3 mm across. These are associated with light brown and reddish brown millimeter-scale mineral grains. The surface has no pitting or staining.

SHERLOC scans of Garde include 0207\_Garde Survey\_15\_1, 0207\_Garde HDR\_500\_1, 0207\_Garde HDR\_500\_2, 0208\_Garde Detail\_500\_1, 0208\_Garde Detail\_500\_2, and 0208\_Garde Detail\_500\_3. The Garde survey scan does not contain any spectra with Raman signals strong enough to assign. The remaining scans contain Raman spectra corresponding to olivine, carbonate, silicate, and perchlorate or phosphate, as well as possible pyroxene (Fig. 3D).

Olivine was the primary mineral we detected in all of the HDR and Detail scans performed on Garde; 21% of the combined 500 points of these scans were definitively assigned to olivine, and an additional 14% were assigned as probable olivine (Fig. 3B-C). The dominant peak in the mean spectrum of all points in 0208\_Garde Detail\_500\_1 assigned to olivine is centered at  $830\text{ cm}^{-1}$ , represented by the vertical green line in figure 3D. The points in Garde assigned to olivine generally fall on the reflective gray-green mineral grains.

We also detected carbonate across all of the Garde HDR and Detail scans, with 7% of the 500 points definitively assigned to carbonate and an additional 11% assigned to probable carbonate (Fig. 3B-C). The dominant peak of the mean spectrum of all points in scan 0208\_Garde Detail\_500\_1 assigned to carbonate is centered at  $1085\text{ cm}^{-1}$ , represented by the vertical cyan line in figure 3D. However, as in the Dourbes carbonate detections, this assignment is to mineral class only, not species. The points assigned to carbonate fall on light brown and reddish brown grains that are closely associated with the olivine grains.

All three of the Garde Detail scans contain Raman spectra that are consistent with perchlorate or phosphate. The dominant peak of a mean spectrum of all points in scan 0208\_Garde Detail\_500\_1 assigned to perchlorate or phosphate is centered at  $956\text{ cm}^{-1}$ , represented by the vertical lavender-blue line in figure 3D. As in Dourbes, this peak falls between the dominant peak of perchlorate and phosphate standards analyzed by SHERLOC analogue instruments (see sections 3.1 and S4.8) and cannot be confidently assigned to either mineral. We did not observe hydration features in the Garde spectra assigned perchlorate/phosphate. The points assigned to perchlorate or phosphate in the Garde Detail scans generally fall on non-reflective light gray grains.

The spectra in scan 0208\_Garde Detail\_500\_1 assigned to perchlorate or phosphate also feature a fluorescence band located at  $\sim 340\text{ nm}$  (Scheller et al., 2022). The  $\sim 340\text{ nm}$  fluorescence feature could result from organic species and/or from trivalent cerium ( $\text{Ce}^{3+}$ ) within a phosphate crystal structure (Shkolyar et al., 2021). The possible presence of ( $\text{Ce}^{3+}$ ) fluorescence may support a phosphate assignment for these spectra. However, the fluorescence spectral assignment is not straightforward (see section S4.6).

Scans 0207\_Garde HDR\_500\_2, 0208\_Garde Detail\_500\_1, and 0208\_Garde Detail\_500\_3 contain points assigned to silicate. The silicate detections fall on dark gray non-reflective grains and are often associated with perchlorate or phosphate detections in the Detail scans (Figs. 3B-C). The mean spectrum of all points in scan 0208\_Garde Detail\_500\_1 assigned to silicate features a broad band centered at  $1057\text{ cm}^{-1}$ , represented by the vertical yellow line in

figure 3D. This band is qualitatively similar to one seen in a labradorite spectrum collected by ACRONM (see section S4.2) SHERLOC also detected possible pyroxene at six points across 0207\_Garde HDR\_500\_1, 0207\_Garde HDR\_500\_2, and 0208\_Garde Detail\_500\_3. The mean spectrum of these six spectra features a peak at  $\sim 1020\text{ cm}^{-1}$ , which most closely matches a spectrum collected from diopside on Brassboard. However, the comparison to a standard diopside spectrum is not a formal mineral assignment, which will require a detailed investigation beyond the scope of this paper.

**Figure 3.** SHERLOC Raman mineral identifications from Garde. A) The abrasion patch imaged by WATSON (image ID SIF\_0206\_0685226491\_804FDR\_N0071836SRLC01024\_0000LMJ01). Yellow boxes indicate the location of scans. B) Colorized (left) and grayscale (right) ACI images (image ID SC3\_0208\_0685436606\_980FDR\_N0071836SRLC11372\_0000LMJ01) of the region of the abrasion patch bounded by the larger yellow box in panel A. The white circles in panel B indicate the locations of SHERLOC analysis spots for scan 0207\_Garde HDR\_500\_2. Mineral identifications are indicated in the right panel. C) Upper Panel: Colorized (left) and grayscale (right) ACI images (image ID SC3\_0208\_0685432316\_968FDR\_N0071836SRLC11370\_0000LMJ01) of the region of the abrasion patch where the Detail scans occurred. The white circles on the grayscale ACI image in panel C indicate the locations of SHERLOC analysis spots of three  $1\text{ mm}^2$  Detail scans. The lower subpanel shows mineral identifications for the Detail scans. D) Representative Raman spectra of minerals detected with high confidence and spectra of mineral standards collected on the SHERLOC Brassboard instrument at JPL. Vertical lines indicate peak centers. Spectra are offset along the y-axis for clarity.

### 3.1.3 Quartier

The Quartier abrasion patch, which was approximately 7 mm deep, was made on sol 292 on Issole, a weathered, tabular outcrop of the Issole member of the Séítah formation, near the contact of the Séítah and Máaz formations (Fig. 1). The pre-abrasion surface of Quartier exhibited multiple textures: centimeter-scale platy features, rounded bumps that were up to approximately one centimeter tall, and a patchy covering of coarse regolith to fine-grained gravel (Fig. S2C). It also featured occasional rounded centimeter-scale pebbles. Quartier is associated with two core samples from the Issole outcrop: Robine and Malay. Abrading Quartier revealed prominent dark gray-to-black angular 1–5 mm mineral grains associated with smaller and less abundant light-to-dark gray minerals that are sometimes rimmed with light reddish-brown material (Fig. 4A). These gray-to-black mineral grains exist within a light colored matrix. The surface also features scattered, irregularly shaped, bright white mineral grains and closely associated reddish-brown mineral grains. SHERLOC scans of Quartier focused on an area that is dominated by bright white and reddish-brown grains, with some dark gray-to-black grains (Figs. 4A and B).

SHERLOC scans of Quartier include 0293\_Quartier Survey\_15\_1, 0293\_Quartier HDR\_500\_1, 0304\_Quartier Survey\_15\_1 (which had  $50\text{ }\mu\text{m}$  spacing), 0304\_Quartier Detail\_500\_1, 0304\_Quartier Detail\_500\_2, 0304\_Quartier Detail\_500\_3, and 0304\_Quartier Detail\_500\_4. (Fig. 4). All of the Quartier scans, including the survey scans, contain spectra that correspond to sulfate. The Quartier HDR and Detail scans also contain spectra corresponding to carbonate, olivine, undefined silicate, perchlorate, and perchlorate or phosphate (Fig. 4B-D).

Carbonate and sulfate were the most abundant minerals detected in 0293\_Quartier HDR\_500\_1 (Fig. 4B). Eighteen percent of the points in this scan were definitively assigned to carbonate and an additional 18% were assigned as probable carbonate. The dominant peak of the mean spectrum of all points in 0293\_Quartier HDR\_500\_1 definitively assigned to carbonate, with no second assignment, is centered at  $1085\text{ cm}^{-1}$ , represented by the vertical cyan line in

figure 2D. Twelve percent of the points were definitively assigned to sulfate and an additional 9% were assigned as probable sulfate. The mean spectrum of all points in 0293\_Quartier HDR\_500\_1 definitively assigned to sulfate has a primary peak centered at  $1011\text{ cm}^{-1}$  and no clear secondary peaks.

The sulfate detections in 0293\_Quartier HDR\_500\_1 are generally collocated with a patch of bright white mineral grains, while the carbonate detections fall on reddish-brown mineral grains surrounding the sulfate grains (Fig. 4B). A single point in this scan was assigned as probable olivine. This detection falls on a highly reflective, light gray mineral that is surrounded by carbonate (Fig. 4B). The spectrum of one point definitively assigned to sulfate in this scan also contains a peak at  $952\text{ cm}^{-1}$  assigned to perchlorate or phosphate. This point falls partially on bright white grains and partially on a small brown grain within the patch of bright white mineral grains (Figs. 4B). Two points in the 0293\_Quartier HDR\_500\_1 scan were definitively assigned to silicate and one point was identified as a probable silicate. The silicate detections fall on dark gray-to-black mineral grains (Fig. 4B).

The four Quartier Detail scans, which were focused on the bright white mineral grains, are dominated by sulfate detections (Figs. 4C). Of the 400 combined points in the Quartier Detail scans, we definitively assigned 66% to sulfate and assigned 11% probable sulfate. As in the HDR scan of Quartier, the sulfate detections were collocated with the bright white mineral grains. The mean spectrum of all points in 0304\_Quartier Detail\_500\_1 definitively assigned to sulfate only has a primary peak centered at  $1015\text{ cm}^{-1}$ , represented by the vertical red line in figure 4D, and secondary peaks at  $1133\text{ cm}^{-1}$  and  $1221\text{ cm}^{-1}$ , represented by dashed and dotted vertical red lines, respectively (Fig. 4D). The primary peak of the representative Quartier sulfate spectrum and the secondary peak at  $1133\text{ cm}^{-1}$  are near the primary and secondary peaks of a gypsum standard (WARDS #46–3798) spectrum collected on Brassboard, which has peaks at  $1009\text{ cm}^{-1}$  and  $1129\text{ cm}^{-1}$  (Fig. 4D). The secondary peak at  $1221\text{ cm}^{-1}$  in the Quartier sulfate spectrum does not correspond to any peak in the Brassboard gypsum spectrum. However, the primary peak in the Quartier sulfate spectrum also has good agreement with the primary peak of the synthetic magnesium sulfate (Macron Chemicals) spectrum collected on Brassboard, which is centered at  $1019\text{ cm}^{-1}$ , and the two secondary magnesium sulfate peaks that can vary between  $\sim 1060\text{ cm}^{-1}$  and  $\sim 1260\text{ cm}^{-1}$ , according to hydration state (Wang et al., 2006; Fig. 4D). The representative Quartier sulfate spectrum has a broad band with two peaks at  $3229\text{ cm}^{-1}$  and  $3415\text{ cm}^{-1}$ , which is consistent with OH stretching mode bands seen in hydrated sulfates (Fig. S10b). Further investigation is needed to establish the primary cation and hydration states of Quartier sulfates at individual points within the Quartier scans, but the mean spectrum presented in figures 4D and S10b suggests that the bright white minerals of Quartier may be a mixture of calcium and magnesium sulfate at various levels of hydration.

In addition to sulfate, the Quartier Detail scans detected carbonate, olivine, perchlorate/chlorate, and perchlorate or phosphate. Three definitive carbonate detections, one in 0304\_Quartier Detail\_500\_1 and two in 0304\_Quartier Detail\_500\_2, fall on small, reddish-brown mineral grains at the margins of sulfate grains within or at the edge of the bright white patch of sulfate. Only one definitive olivine assignment was made in the Quartier Detail scans. It was at a point that was also definitively assigned to sulfate and falls on small, light gray grains at a boundary between dark gray and bright white grains (Fig. 4C). We definitively assigned three points in 0304\_Quartier Detail\_500\_1 to perchlorate or chlorate with unknown cation, all of which were also definitively assigned sulfate. The perchlorate/chlorate assignments were made based on the presence of peaks at  $938\text{ cm}^{-1}$ ,  $935\text{ cm}^{-1}$ , and  $931\text{ cm}^{-1}$ , which are consistent with

the primary peaks in ACRONM spectra collected from several different oxychlorine species (Fig. S12). The points assigned perchlorate/chlorate fall on light gray-to-brown material at the boundary between a bright white and dark gray-to-black grain (Fig. 4C).

We assigned eight points in the Quartier Detail scans to perchlorate or phosphate. Six of these points are also assigned to sulfate, one is also assigned to carbonate, and one is also assigned to both sulfate and carbonate. The perchlorate or phosphate peak in the mean spectrum of the eight perchlorate or phosphate spectra is centered at  $\sim 959\text{ cm}^{-1}$  (Fig. 4D) and cannot be definitively assigned to perchlorate or phosphate (see sections S4.6 and S4.8). Most of these detections are associated with hydrated sulfate detections. The single perchlorate/chlorate detection in 0304\_Quartier Detail\_500\_2 that is not associated with sulfate has no discernable hydration features. Like the points assigned perchlorate/chlorate, these points fall on light gray-to-brown material at the boundaries of bright white mineral grains.

**Figure 4.** SHERLOC Raman mineral identifications from Quartier. A) The abrasion patch imaged by WATSON (image ID SIF\_0292\_0692866773\_550FDR\_N0090000SRLC00702\_0000LMJ01). The yellow box indicates the location of the HDR scan and blue boxes indicate the location of the Detail scans. B) Colorized (left) and grayscale (right) ACI images (image ID SC3\_0293\_0692982585\_671FDR\_N0090000SRLC10600\_0000LMJ01) of the region of the abrasion patch bounded by the larger yellow box in panel A. The white circles in panel B indicate the locations of SHERLOC analysis spots for 0293\_Quartier HDR\_500\_1. Mineral identifications are indicated in the right panel. C) Colorized (bottom left) and grayscale (bottom right) ACI (image ID SC3\_0304\_0693962423\_667FDR\_N0090000SRLC11373\_0000LMJ01) images of the region of the abrasion patch where the Detail scans occurred. The white circles on the grayscale ACI image in panel C indicate the locations of SHERLOC analysis spots for four  $1\text{ mm}^2$  Detail scans. The other four subpanels show mineral identifications for Quartier Detail scans. D) Representative Raman spectra of minerals detected with high confidence from the abrasion patch and spectra of mineral standards collected on the SHERLOC Brassboard instrument at JPL. Vertical lines represent peak centers. Spectra are offset along the y-axis for clarity.

## 3.2 Mááz Targets

### 3.2.1 Guillaumes

Guillaumes was the first abraded patch of the Mars 2020 mission, made on sol 160. This abrasion, which was approximately 8 mm deep, was on a low-relief, polygonal outcrop of the Roubion member of the Mááz formation, also called Roubion (Fig. 1). The pre-abrasion surface of the target appeared degraded, granular, and flaky, with regolith embedded in the lowest points and rounded pebbles up to  $\sim 5\text{ mm}$  in size across it (Fig. S2D). Meter-scale, friable, low-relief, polygonal outcrops are characteristic of the Roubion member, which is at least  $\sim 5\text{ m}$  thick and interpreted to be the stratigraphically lowest member of the Mááz formation (Farley et al., 2022). The attempt to core this target produced a borehole and cuttings, but no core was recovered (Simon et al., 2022). The Guillaumes abrasion (Fig. 5A) revealed millimeter-scale, interlocking, light and dark mineral grains. Slightly larger, irregularly shaped bright white mineral grains were also present. The abraded surface featured pits and crevices up to approximately 5 mm in diameter. The surface was discontinuously stained by dark brown material, particularly in and near the pits.

SHERLOC Guillaumes scans included 0161\_Guillaumes Survey\_15\_1, 0161\_Guillaumes HDR\_100\_1, 0161\_Guillaumes HDR\_100\_2, 0161\_Guillaumes HDR\_300\_1, 0162\_Guillaumes HDR\_250\_1 and 0162\_Guillaumes HDR\_250\_2. The sol 161 scans covered an area of the abraded surface that was primarily composed of interlocking light and dark mineral grains with extensive dark brown staining while the sol 162 scans covered an area of



interlocking light and dark grains with both irregular bright white mineral grains and discontinuous dark brown staining (Figs. S3A-C, 5A-B).

The sol 161 scans yielded only two spectra with Raman peaks that could be assigned to a mineral class (Fig. S3A-B). The limited Raman signal observed in this scan may be the result of iron oxide minerals coating much of the area this scan covered, which is suggested by the brown staining on the abraded surface (Figs. S3A-B, 5A). The two assigned points are point ten of 0161\_Guillaumes HDR\_100\_2 and point ten of 0161\_Guillaumes HDR\_300\_1, which are approximately collocated; both are assigned to perchlorate with an unknown cation.

In the sol 162 scans, we observed numerous spectra of sodium perchlorate, perchlorate with no cation assignment, and sulfate, in agreement with Scheller et al. (2022), along with a single possible silicate spectra (Figs. 5, S3). The perchlorate and sulfate detections generally fall on irregular bright white mineral grains. The representative Guillaumes sodium perchlorate spectrum in figure 5C is the mean spectrum of the points in scan 0162\_Guillaumes HDR\_250\_1 assigned to sodium perchlorate with no second assignment (Fig 5B). The dominant peak of this spectrum is centered at  $952\text{ cm}^{-1}$ , represented by the vertical solid blue line in figure 5C. The secondary peaks in this spectrum are centered at  $1091\text{ cm}^{-1}$  and  $1150\text{ cm}^{-1}$ , represented by vertical dashed and vertical dotted blue lines in figure 5C, respectively. The signal to noise ratios of both the primary and secondary peaks in the individual Guillaumes spectra assigned to sodium perchlorate were greater than ten. For SHERLOC spectra with  $S/N > 10$ , the standard deviation of the fitted peak position error is less than  $1.2\text{ cm}^{-1}$  (see section S1). As a result, we can confidently assign these Guillaumes detections to a specific mineral species. The peaks of the representative Guillaumes sodium perchlorate spectrum directly correspond to the peaks of the sodium perchlorate (Sigma Aldrich 310514) standard spectrum collected on the Brassboard. In addition to peaks at  $\sim 950\text{ cm}^{-1}$ ,  $\sim 1090\text{ cm}^{-1}$ , and  $\sim 1150\text{ cm}^{-1}$ , the Brassboard spectrum features a hydration peak centered at  $\sim 3500\text{ cm}^{-1}$  that is approximately three times as intense as the peak at  $\sim 1090\text{ cm}^{-1}$ . We did not observe a potential hydration peak in any individual or averaged Guillaumes sodium perchlorate spectra.

The representative Guillaumes perchlorate spectrum in figure 5C is the mean spectrum of the points in scan 0162\_Guillaumes HDR\_250\_1 definitively assigned to perchlorate with no second assignment (Fig 5B). The dominant peak of this spectrum is centered at  $950\text{ cm}^{-1}$ . Secondary peaks were not discernible in individual spectra assigned to perchlorate with unknown cation. However, the mean spectrum displays a weak peak at  $\sim 1090\text{ cm}^{-1}$ , which corresponds to the most intense secondary peak in the Brassboard spectrum, and the primary peak corresponds to the primary sodium perchlorate peak, suggesting that the perchlorate spectra represent weak sodium perchlorate detections. This mean spectrum also exhibits a weak peak that corresponds with the primary peak of the sulfate spectra detected in Guillaumes, which demonstrates the close association of perchlorate and sulfate in this target.

The representative Guillaumes sulfate spectrum in figure 5C is the mean spectrum of the points in scan 0162\_Guillaumes HDR\_250\_1 assigned to sulfate with no second assignment (Fig. 5). The dominant peak of this spectrum is centered at  $1017\text{ cm}^{-1}$  and the secondary peak is centered at  $1123\text{ cm}^{-1}$ , represented by the solid and dashed vertical red lines in figure 5C, respectively. This spectrum also exhibits a weak, broad OH stretching band with two peaks at  $3287\text{ cm}^{-1}$  and  $3498\text{ cm}^{-1}$ . Similarly to the sulfate spectra observed in Quartier scans, peak positions in the representative Guillaumes sulfate spectrum are consistent with some features of several different Brassboard sulfate spectra, including gypsum, epsomite (CVS epsom salts), natural kieserite (JPL mineral collection), and synthetic magnesium sulfate (Macron Chemicals).

This suggests that the sulfates detected in Guillaumes may have mixed calcium and magnesium cations, but further investigation is needed before mineral species assignments are made. The mean Guillaumes sulfate spectrum also features a weak peak that corresponds with the primary perchlorate peak, again demonstrating the close association of these two minerals in Guillaumes.

**Figure 5.** SHERLOC Raman mineral identifications from scan 0162\_Guillaumes HDR\_250\_1. A) The abrasion patch imaged by WATSON (image ID S11\_0160\_0681181210\_679FDR\_N0060000SRLC00003\_000095J01). Yellow boxes indicate the location of the scans performed. The left box corresponds to HDR scans performed on sol 161 (Fig. S3). The right box corresponds to HDR scans performed on sol 162. B) colorized (left) and grayscale (right) ACI images (image ID SC3\_0162\_0681352993\_195FDR\_N0060000SRLC11420\_0000LMJ01) of the region of the abrasion patch bounded by the right yellow box in panel A. The white circles in panel B indicate the locations of SHERLOC analysis spots. Mineral identifications from scan 0162\_Guillaumes HDR\_250\_1 are indicated in the right panel. C) Representative Raman spectra of minerals detected with high confidence from the abrasion patch and spectra of mineral standards collected on the SHERLOC Brassboard instrument at JPL. Vertical lines indicate peak centers. Spectra are offset along the y-axis for clarity.

### 3.2.2 Foux

SHERLOC scanned the natural target Foux on sol 141. SHERLOC also scanned two other natural targets during the Crater Floor Campaign (see section 3.2.5). Like Guillaumes, Foux was a low-relief, polygonal outcrop of the Roubion member of the Mááz formation. Its surface was somewhat similar to the unabraded surface of Guillaumes. It appeared degraded and had regolith settled into its recesses. It also featured occasional rounded pebbles, up to ~5 mm in size (Fig. S2E). The most notable difference between the surface of Foux and the unabraded surface of Guillaumes was the presence of a purplish coating on Foux (Garczynski et al., 2022).

Scans of Foux included 0141\_Foux Survey\_15\_1, 0141\_Foux HDR\_100\_1, 0141\_Foux HDR\_100\_2, and 0141\_Foux HDR\_300\_1. As in the other two natural targets of the Crater Floor Campaign, Nataani and Bi La Sana (see section 3.2.5), but unlike scans of the abraded targets, the Foux scans produced no single Raman spectra that could be given a mineral assignment. This was expected, as SHERLOC is optimized for analyzing dust-free surfaces with low relief, conditions that were not met on the surface of Foux, Nataani or Bi la Sana. The median and average spectra of all of the Foux scans showed silicate bands centered between ~1040  $\text{cm}^{-1}$  and ~1050  $\text{cm}^{-1}$  (Fig. S5) and the fused silica background spectral signature peaks at ~480  $\text{cm}^{-1}$  and ~800  $\text{cm}^{-1}$  discussed in section 2.4 (Fig. S4b).

### 3.2.3 Montpezat

The Montpezat abrasion, which was approximately 8 mm deep, was made on sol 346 on Rimplas, an outcrop of the Artuby member of the Mááz formation. The surface of Rimplas is coarse-grained and exhibits 1–10 centimeter thick layers with variable erosion resistance between layers (Fig. 1). A coarse-grained surface texture and decimeter thick layers are characteristic of the Artuby member (Farley et al., 2022). The pre-abrasion surface of the Montpezat target looked very similar to that of Guillaumes and Foux, with coarse regolith and fine gravel packed into recesses between bumps up to ~5mm tall, occasional, rounded, sub-centimeter pebbles, and small patches of purplish coating (Fig. S2F). Rimplas was not an intended coring target and the Montpezat abrasion is not associated with any sample cores.

The abraded surface of Montpezat appears highly altered compared to that of the other abraded targets (Fig. 6A). It is uneven, perhaps due to pitting that is similar to but more extensive than that seen on Guillaumes. The surface also exhibits extensive staining with dark brown-to-

black material. Furthermore, it is partially covered in fine material that is likely cuttings from the abrasion process, possibly because the gDRT used a smaller volume of nitrogen gas to clean Montpezat than it used for previous targets. The least altered or occluded portion of the surface of Montpezat was targeted for SHERLOC scanning, but there is reddish brown staining over much of the scanned surface. The scanned surface exhibits sub-millimeter to millimeter sized interlocking white to dark gray-blue grains.

SHERLOC scans of Montpezat included 0349\_Montpezat Survey\_15\_1 and 0349\_Montpezat HDR\_500\_1 scans. No points in the Montpezat Survey scan had a discernible Raman signal. The 0394\_Montpezat HDR\_500\_1 scan revealed silicate, carbonate, and perchlorate or phosphate spectral signatures. Seventeen single spectra display silicate signatures, however, only four of those assignments were made with high confidence. We observed three carbonate and three perchlorate or phosphate spectra in the scan. All carbonate spectra and one of the perchlorate or phosphate spectra are of low confidence. Figure 6C shows the mean spectrum of all 0349\_Montpezat HDR\_500\_1 definitively assigned to silicate and the mean spectrum of the two points definitively assigned to perchlorate or phosphate. These peaks are centered at 1050  $\text{cm}^{-1}$  and 959  $\text{cm}^{-1}$  respectively. The Montpezat HDR scan also contains one spectrum with a low, broad band centered at  $\sim 1600 \text{ cm}^{-1}$ , which may be a graphitic (G) band. The point with the possible G band is indicated by a capital G on a white background in figure 6B. A report from the SHERLOC team that discusses the context and implications of this detection is forthcoming.

**Figure 6.** SHERLOC Raman mineral identifications from the 0349\_Montpezat HDR\_500\_1 scan of target Montpezat. A) The abrasion patch imaged by WATSON (image ID SIF\_0346\_0697661461\_972FDR\_N0092982SRLC01034\_0000LMJ01). The yellow box indicates the location of the scan. B) Colorized (left) and grayscale (right) ACI images (image ID SC3\_0349\_0697954126\_179FDR\_N0092982SRLC10600\_0000LMJ01) of the region of the abrasion patch bounded by the yellow box in panel A. The white circles in panel B indicate the locations of SHERLOC analysis spots. Mineral identifications are indicated in the right panel. C) Representative Raman spectra from the abrasion patch of minerals detected with high confidence, and mineral standard spectra collected on the SHERLOC Brassboard instrument at JPL and the ACRONM instrument at JSC. Spectra are offset along the y-axis for clarity.

### 3.2.4 Bellegarde

The Bellegarde abrasion, which was approximately 8 mm deep, was made on sol 185 on a small blocky boulder (approximately 40 cm across; Fig. 1) of the Rochette member of the Máaz formation. The boulder was chosen as the second target for abrasion and coring in part because it did not appear to be highly weathered (Fig. S2G), indicating a high likelihood for successful core recovery. In fact, the first two successful cores of the Mars 2020 mission, Montdenier and Montagnac, were retrieved from this boulder (Simon et al., 2022). The erosion-resistant Rochette member is approximately 30 to 50 cm thick and often exhibits centimeter scale layering (Farley et al., 2022). The Rochette member caps the crest of Artuby ridge (Sun et al., 2022).

The abraded surface of Bellegarde (Fig. 7A) features sub-millimeter, interlocking, white to dark green-gray mineral grains. We also observed some larger, bright white mineral grains rimmed by a tan material on the surface of Bellegarde. The surface of Bellegarde is partially stained by a reddish-brown material.

SHERLOC scans of Bellegarde include 0186\_Bellegarde Survey\_15\_1, 0186\_Bellegarde HDR\_250\_1, and 0186\_Bellegarde HDR\_250\_2. The data from these scans indicate that Bellegarde contains silicate, perchlorate or phosphate, and sulfate spectral signatures. As reported by Scheller et al. (2022), the Bellegarde Survey scan detected sulfate associated with the

largest cluster of bright white minerals in the upper left region of the scan. Only 17 of 200 total spectra across both Bellegarde HDR scans show Raman spectral signatures. The low level of Raman signals in Bellegarde may be due to the presence of iron oxide minerals at the target surface, which is suggested by the reddish-brown staining. Most Bellegarde mineral detections are on regions of the target that have no staining.

The 17 mineral detections in the Bellegarde HDR scans include three definitive and seven probable silicate, which fall on dark gray grains; four probable sulfate, which are only sometimes associated with bright white grains; and two definitive and one probable perchlorate or phosphate, which fall on medium to dark gray grains. Figure 7C shows the mean spectrum of all 0186\_Bellegarde HDR\_250\_2 definitively assigned to silicate and the mean spectrum of the two points definitively assigned to perchlorate or phosphate. These peaks are centered at 1036  $\text{cm}^{-1}$  and 955  $\text{cm}^{-1}$  respectively. The peak centered at 1036  $\text{cm}^{-1}$  is qualitatively similar to the band in a labradorite spectrum collected by ACRONM and assigned to silicate (Fig. 7C).

As in Garde, the Bellegarde spectra assigned to perchlorate or phosphate also feature a fluorescence band at  $\sim 340$  nm (Scheller et al., 2022). The  $\sim 340$  nm fluorescence feature could result from organic species and/or from trivalent cerium ( $\text{Ce}^{3+}$ ) within a phosphate crystal structure (Shkolyar et al., 2021). Therefore, the  $\sim 340$  nm fluorescence feature may support a phosphate assignment for these detections (see section S4.6). Data acquired by Perseverance's SuperCam instrument revealed the presence of an anhydrous sodium perchlorate signature associated with a bright white patch of mineral grains at Bellegarde that was not analysed by SHERLOC, similar to that detected by both SHERLOC and SuperCam at Guillaumes (see section 3.2.1; Meslin et al., 2022). Taken together, these analyses suggest that both phosphate and perchlorate may be present in the Bellegarde abrasion.

**Figure 7.** SHERLOC Raman mineral identifications from scan 0186\_Bellegarde HDR\_250\_2 of the target Bellegarde. A) The abrasion patch imaged by WATSON (image ID SIF\_0185\_0683368184\_652FDR\_N0070000SRLC00720\_0000LMJ01). The yellow box indicates the location of the HDR. B) Colorized (left) and grayscale (right) ACI images (image ID SC3\_0186\_0683479674\_054FDR\_N0070000SRLC11420\_0000LMJ02) of the region of the abrasion patch bounded by the yellow box in panel A. The white circles in panel B indicate the locations of SHERLOC analysis spots. Mineral identifications are indicated in the right panel. C) Representative Raman spectra from the abrasion patch of minerals detected with high confidence, and mineral standard spectra collected on the SHERLOC Brassboard instrument at JPL and the ACRONM instrument at JSC) Vertical lines indicate peak centers. Spectra are offset along the y-axis for clarity.

### 3.2.5 Nataani and Bi la Sana

SHERLOC's first two sets of scans on Mars were performed on the natural targets Nataani, on sol 83, and Bi la Sana, on sol 98 (Fig. S2H-I). These targets are expressions of the Nataani member of the Mááz formation, which overlies the Rochette member, according to ground penetrating radar data (Farley et al., 2022).

Scans on Nataani included 0083\_Nataani Survey\_10\_1, which yielded no detectable Raman signal; 0083\_Nataani HDR\_5\_1, which yielded no detectable Raman signal; 0083\_Nataani HDR\_50\_1, which displayed the fused silica background peaks at  $\sim 480$   $\text{cm}^{-1}$  and  $800$   $\text{cm}^{-1}$  (see sections 2.4 and S2) in the mean and median spectra; and 0083\_Nataani HDR\_100\_1, which displayed the fused silica background signal and an silicate band centered at

~1055 cm<sup>-1</sup> in the mean and median spectra (Fig. S5). Unlike most survey scans in the Crater Floor Campaign, which had 144 μm spacing, 0083\_Nataani Survey\_10\_1 had 200 μm spacing.

The sol 98 set of scans of the natural target Bi la Sana included 0098\_Bi la Sana Survey\_15\_1, 0098\_Bi la Sana HDR\_100\_1, 0098\_Bi la Sana HDR\_100\_2, and 0098\_Bi la Sana HDR\_300\_1. All Bi la Sana scans displayed the fused silica background signal and an silicate band centered at ~1050 cm<sup>-1</sup> in the mean and median spectra (Fig. S5).

While Raman mineral detections were minimal in the natural target scans of the Crater Floor Campaign, compared to the abraded target scans, it is noteworthy that the same silicate signature observed in many abraded target scans also appears in several of the natural target scans.

### 3.2.6 Alfalfa

The Alfalfa abrasion, which was approximately 9 mm deep, was made on sol 367 on Sid, a boulder in the Ch'ał member of the Máaz formation (Fig. 1). The Ch'ał member overlies the Nataani member (Farley et al., 2022) Sid is a blocky, apparently structureless, gray boulder and a typical representative of the Ch'ał member. The light tan-to-gray pre-abrasion surface of Sid was polished and fluted by wind abrasion and relatively dust free (Fig. S2J). Two core samples, Ha'ahóni and Atsá, were retrieved from Sid. The Alfalfa abrasion revealed interlocking, sub-millimeter to ~ 5 mm bright white, brown, gray, and black mineral grains (Fig. 8A). The largest of the grains are bright white, lath-like, and highly reflective. There is patchy reddish brown coloration across the entire abraded surface.

SHERLOC scans of Alfalfa include 0370\_Alfalfa Survey\_15\_1 and 0370\_Alfalfa HDR\_500\_1. The Alfalfa scans contain predominantly silicate spectra with minor components of carbonate and perchlorate or phosphate. In the single HDR Raman scan collected on alfalfa, silicate comprised 44 of the 100 spectra with 30 detections of high confidence. The mean spectrum of the definitive silicate detections contains a broad band centered at 1053 cm<sup>-1</sup>, which is qualitatively similar to a broad band in a labradorite spectrum collected by ACRONM (Fig. 8C). Carbonate and perchlorate or phosphate peaks were found in 5 and 3 spectra respectively. Two of the perchlorate or phosphate assignments were of high confidence and only one of the carbonate assignments was of high confidence. The mean spectrum of the two definitively assigned perchlorate or phosphate detections has a peak centered at 949 cm<sup>-1</sup> (Fig. 8C).

Several of the silicate detections are associated with bright white, highly reflective mineral grains, including a large lath-like crystal. This mineral morphology suggests that the Alfalfa silicate detections may be plagioclase feldspar minerals. The carbonate detections fall on light brown to red regions of the surface and the perchlorate or phosphate detections appear to fall at the margins of angular, black mineral grains. No mineral detections fell on the reddest regions of the target surface, which may indicate that the red color is the result of the presence of iron cations (Fig 8B), since ferric iron cations can absorb DUV laser radiation (Morris et al., 2022; Razzell Hollis et al., 2021a and b).

**Figure 8.** SHERLOC Raman mineral identifications from scan 0370\_Alfalfa HDR\_500\_1 of target Alfalfa. A) The abrasion patch imaged by WATSON (image ID SIF\_0367\_0699544277\_375FDR\_N0110108SRLC08029\_0000LMJ01). The yellow box indicates the location of the Alfalfa HDR scan. B) Colorized (left) and grayscale (right) ACI images (image ID SC3\_0370\_0699816293\_742FDR\_N0110108SRLC10600\_0000LMJ01) of the region of the abrasion patch bounded by the yellow box in panel A. The white circles in panel B indicate the locations of SHERLOC analysis spots. Mineral identifications are indicated in the right panel. C) Representative Raman spectra from the abrasion patch of minerals,

and mineral standard spectra collected on the SHERLOC Brassboard instrument at JPL and the ACRONM instrument at JSC. Vertical lines indicate peak centers. Spectra are offset along the y-axis for clarity.

## 4 Discussion

SHERLOC scans of the three abraded Séítah targets and four abraded Mááz targets described above support the conclusions that the Séítah unit is an olivine cumulate and Mááz is a less mafic igneous unit. In addition, the SHERLOC scans reveal that, between them, the Séítah and Mááz units may record the histories of at least three different aqueous alteration events on the floor of Jezero Crater, including olivine carbonation and sulfate dominated salt deposition in Séítah, and sodium perchlorate dominated salt deposition in Mááz. The iron oxides present on the four Mááz targets (Wiens et al., 2022) are also likely the result of aqueous alteration. Ultimately, the data acquired by SHERLOC during the Crater Floor Campaign show evidence that Jezero Crater was once a chemically active aqueous environment with the potential to host and preserve evidence of microbial life.

Figure 9 shows that the three most common mineral class detections in SHERLOC scans of Séítah targets were olivine, carbonate, and sulfate. Olivine and carbonate detections dominated scans in targets Dourbes and Garde, while minimal olivine was detected in Quartier. Scans of Quartier and Dourbes both revealed patches of sulfate, while Garde scans detected no sulfate. The minimal olivine detections in Quartier and lack of sulfate detection in Garde may not reflect a major difference in the mineralogy of these targets. The discrepancies may, instead, reflect the SHERLOC team's decision to focus Quartier scans on the bright white patches of the target and the patchy nature of salt deposits in the Séítah formation.

We observe gray grains similar to the one that corresponds with a definitive olivine spectrum in 0304\_Quartier Detail\_500\_1 across the surface of Quartier, sometimes rimmed by light reddish-brown material (Fig. 4A). These gray grains appear similar to grains identified as olivine in Dourbes and Garde and the reddish-brown material looks similar to carbonate that was associated with the olivine in Dourbes and Garde (Figs. 2, 3). While it is possible that Bastide, the outcrop that hosted the Garde abrasion (Fig. 1), contains no sulfate deposits, it is equally likely that the Garde abrasion and scans simply did not sample Bastide's sulfate deposits. As demonstrated by the sulfate detected in Dourbes (Fig. 2), Séítah sulfate deposits are not all as visually prominent as the sulfate detected in Quartier (Figs. 4).

The closely associated olivine and carbonate detections in Garde and Dourbes suggest that the olivine cumulate Séítah unit was exposed to at least one aqueous alteration event, during which partial carbonation of olivine took place (Figs. 2 and 3). In particular, detail maps of Dourbes reveal a euhedral olivine crystal with no directly associated carbonate sitting less than one millimeter away from a subhedral olivine grain with adjacent carbonate grains (Fig. 2C). Sulfate deposits in both Dourbes and Quartier are rimmed by carbonate that is both spectrally and morphologically similar to the carbonate associated with olivine in Dourbes and Garde (Figs. 2, 3, 4). This suggests that all of the carbonates in Séítah formed via the same process, olivine carbonation, and that Séítah's sulfate was deposited later by a sulfate-rich brine, in pore space generated during olivine carbonation through cracking caused by the pressure of carbonate crystal formation (e.g., Xing et al., 2018).

**Figure 9.** A) This graph presents, for each abraded target of the Crater Floor Campaign, the percent of detections of each mineral class out of the total SHERLOC mineral detections per target. Each group of bars associated with each target adds up to 100 percent. Data are presented in this way to correct for the differences in Raman signal intensities between targets discussed in section 4.1. Séítah formation targets are on the left (Quartier, Garde, and Dourbes) and Mááz targets are on the right (Guillaumes, Bellegarde, Montpezat, and Alfalfa).

Figure 9 shows that the three most common mineral detections in SHERLOC scans of Mááz targets were silicate, sodium perchlorate, and sulfate. It is important to note the widespread presence of iron oxides in Mááz (Wiens et al., 2022). Iron oxides can absorb deep UV laser radiation and attenuate the spectral signatures of any underlying material (Razzell Hollis et al., 2021a; Morris et al., 2022). In all four of the Mááz targets, mineral detections are negatively correlated with the red-to-brown material on their surfaces, which appears consistent with the presence of iron oxide (Figs. 5-8). This indicates that SHERLOC's mineral detections in the Mááz formation were limited by the absorption of DUV laser radiation by iron oxide.

Farley et al. (2022) report that the totality of data collected during the Mars 2020 Crater Floor campaign indicates that the Mááz and Séítah units either originated from two different sources or represent different layers of a single differentiated magma body. The different rock-forming mineral detections of (non- olivine or pyroxene) silicate in the Mááz targets Bellegarde, Montpezat, and Alfalfa, and olivine and pyroxene detections in Séítah targets further supports Farley et al.'s interpretation (Fig. 9).. SHERLOC's microscale mapping of Mááz targets reveals that similar spectra assigned to silicate correspond to grains with very different morphologies. Silicate detections in Montpezat and Bellegarde map to sub-millimeter dark blue-gray grains; in Alfalfa, the detections correspond to mm-scale reflective white lathe-like crystals (Figs. 6-8). Although the (non- olivine or pyroxene) silicate spectra reported above were all compared to the same standard labradorite spectrum, the broad bands that led us to assign the spectra to silicate are centered at different wavenumbers:  $1050\text{ cm}^{-1}$ ,  $1036\text{ cm}^{-1}$ , and  $1053\text{ cm}^{-1}$  in Montpezat, Bellegarde, and Alfalfa, respectively. The variable grain morphology and Raman band placement in Mááz silicate detections suggests that they correspond to at least two different silicate mineral species, and some may actually be amorphous silica detections.

Perchlorate and sulfate detected in Guillaumes and Bellegarde scans are evidence of a third possible aqueous alteration event on the floor of Jezero Crater. While the Guillaumes and Bellegarde salt deposits are similar in morphology to the deposits in Dourbes and Quartier, they differ in mineralogy. The deposits in Dourbes and Quartier were predominantly sulfate, with only minor perchlorate contributions (see sections 3.1.1 and 3.1.3). In contrast, SHERLOC mineral detections on the white patch of minerals in Guillaumes were dominated by perchlorate that can, in some cases, be identified as sodium perchlorate, with lesser, but still significant, sulfate contributions (see section 3.2.1). SHERLOC scans of Bellegarde detected definitive sulfate signatures alongside perchlorate or phosphate signatures and SuperCam detected a definitive sodium perchlorate signature (Meslin et al., 2022; see section 3.2.4). Taken together, these SHERLOC and PIXL detections suggest that the salts in Guillaumes and Bellegarde precipitated from a perchlorate-sulfate-bearing brine as it percolated through the Mááz formation rocks.

The mineral detections discussed above are consistent with a changing, habitable aqueous environment that was capable of supporting microbial life and preserving evidence of that life, if it existed. In low-temperature terrestrial environments, carbonation of mafic to ultramafic rocks, which SHERLOC data from Séítah formation targets indicate occurred in the Jezero Crater lake, produces hydrogen that can fuel low-density microbial communities (e.g. Fones et al., 2019; Twing et al., 2017; Woycheese et al., 2015). Terrestrial sulfate and perchlorate brines, similar to the brines that likely deposited the sulfate and perchlorate that SHERLOC detected in Jezero Crater, can host microbial life (e.g., Cesur et al., 2022; Fox-Powell & Cockell., 2018; Heinz et al., 2019, 2020). Furthermore, terrestrial sulfate minerals can trap and preserve organic

molecules within their structure (eg., Aubrey et al., 2006; Kotler et al., 2008; Schopf et al., 2012; Shkolyar and Farmer, 2018), and halite- and perchlorate-rich hypersaline subsurface deposits in the Atacama Desert can preserve organic molecules for millions of years (Fernández-Remolar et al., 2013).

## 5 Conclusions

During the Mars 2020 Crater Floor Campaign, SHERLOC was the first Raman spectrometer to map mineral composition in context on the surface of another planetary body. The microscale mineral maps of abraded Séítah and Mááz targets SHERLOC produced during this campaign reveal differing igneous protoliths with aqueous alteration histories indicating that the Jezero crater floor was once a habitable aqueous environment and highlight the importance of the proposed Mars Sample Return mission.

SHERLOC data acquired during the Crater Floor Campaign allowed us to identify evidence of olivine carbonation, a process capable of supporting terrestrial microbial metabolic processes (e.g. Fones et al., 2019; Twing et al., 2017; Woycheese et al., 2015), and units bearing sulfate and perchlorate salts, which are known to preserve organic molecules over long periods of time in terrestrial Mars analogue environments (Aubrey et al., 2006; Kotler et al., 2008; Fernández-Remolar et al., 2013; Schopf et al., 2012; Shkolyar and Farmer, 2018). These mineral assignments were made with high confidence, and suggest that the return of Crater Floor Campaign samples associated with Dourbes (Salette or Coulettes) and Quartier (Robine or Malay) in Séítah, where we observed evidence of both olivine carbonation and sulfate deposition, and Bellegarde (Montdenier or Montagnac) in Mááz, where we observed evidence of perchlorate and sulfate deposition, could bring preserved evidence of microbial life that may have existed in Jezero Crater.

SHERLOC scans performed on the floor of Jezero Crater also yielded data that does not allow for straightforward phase assignments, such as the apparent detections of silicate signatures that are common, but associated with differing rock textures, in the Mááz targets Montpezat, Bellegarde, and Alfalfa. Return of Crater Floor Campaign samples associated with Bellegarde (Montdenier or Montagnac) and Alfalfa (Ha'ahóni or Atsá) will allow for laboratory analyses of the sub-millimeter dark blue-gray grains in Bellegarde and large, reflective, lath-like, white grains in Alfalfa that will provide more definitive, fine scale phase identifications that will facilitate an understanding of the discrepancies in silicate mineral detections between SHERLOC and other Perseverance instruments.

## Acknowledgments

We thank the entire Perseverance rover team. The work described in this paper was partially carried out at the Jet Propulsion Laboratory, California Institute of Technology, under a contract with the National Aeronautics and Space Administration. Funding: A.C. was supported by a National Science Foundation Graduate Research Fellowship (award number 2035701). Funding for R.S.J was provided as an Advanced Curation project run by the NASA Astromaterials Acquisition and Curation Office, Johnson Space Center. ADC and AC were supported by the Mars 2020 Returned Sample Science Participating Scientist Program (NASA award number 80NSSC20K0237). EAC thanks the Canadian Space Agency (grant #EXPCOI4) and the Natural Sciences and Engineering Research Council (grant #RGPIN-2021-02995). E.L.S. was supported by a NASA Earth and Space Science Fellowship (NESSF) (grant 80NSSC18K1255)



and the SHERLOC Co-I funds of B.L.E. J.R.H. was supported by a NASA Postdoctoral Program fellowship. J.R.H., A.S., L.W.B., R.B., P.G.C., M.F., F.M.M., and A.S.B. were supported by the 107415 Mars 2020 Phase-E. A.J.W. was supported by the NASA M2020 Participating Scientist Program. T.F. was supported by the Italian Space Agency (ASI) grant agreement ASI/INAF n. 2017-48-H-0. S.S. acknowledges funding from the Swedish National Space Agency (contracts 137/19 and 2021-00092). This work was supported in part by the ISFM Mission Enabling Work Package and the Johnson Space Center. Author contributions: Entire team performed data analysis and interpretation and participated in editing this manuscript. A.C. and R.S.J. contributed equally to the manuscript. Special thanks go to E.L.B. for figure making. L.W.B. and R.B. are the principal and deputy investigators of the SHERLOC instrument. Competing interests: We declare no competing interests.

### Open Research

The data used for the study are available on NASA's Planetary Data System (Beegle et al., 2021).

### References

Abbey, W. J., Bhartia, R., Beegle, L. W., DeFlores, L., Paez, V., Sijapati, K., Sijapati, S., Williford, K., Tuite, M., Hug, W., & Others. (2017). Deep UV Raman spectroscopy for planetary exploration: The search for in situ organics. *Icarus*, 290, 201–214.

Adcock, C. T., Hausrath, E. M., Forster, P. M., Tschauer, O., & Sefein, K. J. (2014). Synthesis and characterization of the Mars-relevant phosphate minerals Fe- and Mg-whitlockite and merrillite and a possible mechanism that maintains charge balance during whitlockite to merrillite transformation. *American Mineralogist*, 99(7), 1221–1232.

<https://doi.org/10.2138/am.2014.4688>

Aubrey, A., Cleaves, H. J., Chalmers, J. H., Skelley, A. M., Mathies, R. A., Grunthaner, F. J., Ehrenfreund, P., & Bada, J. L. (2006). Sulfate minerals and organic compounds on Mars. *Geology*, 34(5), 357. <https://doi.org/10.1130/G22316.1>

Beegle, L. W., Bhartia, R., Deen, Robert G., Padgett, D., Algermissen, S., Dunn, A. E., Toole, N. T., Crombie, M. K., Arena, N. W., Oij, S. L., Abarca, H. E., Slavney, S. (2021). Mars 2020 SHERLOC Bundle. NASA Planetary Data System. <https://doi.org/10.17189/1522643>

Bhartia, R., Beegle, L. W., DeFlores, L., Abbey, W., Razzell Hollis, J., Uckert, K., et al. (2021). Perseverance's Scanning Habitable Environments with Raman and Luminescence for Organics and Chemicals (SHERLOC) Investigation. *Space Science Reviews*, 217, 58.

<https://doi.org/10.1007/s11214-021-00812-z>

Bhartia, R., Hug, W. F. and Reid, R. D. (2012). Improved sensing using simultaneous deep UV Raman and fluorescence detection. Proc. SPIE 8358, *Chemical, Biological, Radiological, Nuclear, and Explosives (CBRNE) Sensing XIII*, 83581A <https://doi.org/10.1117/12.920170>

Brown, A. J., Wiens, R. C., Maurice, S., Uckert, K., Tice, M., Flannery., D., et al. (2022). A Komatitite succession as an analog for the olivine bearing rocks at Jezero (abstract). 53rd Lunar and Planetary Science Conference.

Buzgar, N., & Apopei, A. I. (2009). The Raman study of certain carbonates. *Geologie*, 55(2).

<https://doi.org/10.13140/2.1.1358.3368>

Buzgar, N., Buzatu, A., & Sanislav, I. V. (2009). The Raman study of certain sulfates. *Analele Stiintifice Ale Universitatii Al. I. Cuza*, 55, 5–23.

Carrier, B. L., Abbey, W. J., Beegle, L. W., Bhartia, R., & Liu, Y. (2019). Attenuation of Ultraviolet Radiation in Rocks and Minerals: Implications for Mars Science. *Journal of Geophysical Research: Planets*, 124(10), 2599–2612. <https://doi.org/10.1029/2018JE005758>

Cesur, R. M., Ansari, I. M., Chen, F., Clark, B. C., & Schneegurt, M. A. (2022). Bacterial Growth in Brines Formed by the Deliquescence of Salts Relevant to Cold Arid Worlds. *Astrobiology*, 22(1), 104–115. <https://doi.org/10.1089/ast.2020.2336>

Chopelas, A. (1991.). Single crystal Raman spectra of forsterite, fayalite, and monticellite. *American Mineralogist*, 76(7-8), 1101-1109.

Currie, K. L., Knutson, J., Temby, P. A. (1992). The Mud Tank carbonatite complex, central Australia-an example of metasomatism at mid-crustal levels. *Contributions to Mineralogy and Petrology*, 109(3).

Edgett, K. S., Yingst, R. A., Ravine, M. A., Caplinger, M. A., Maki, J. N., Ghaemi, F. T., Schaffner, J. A., Bell, J. F., Edwards, L. J., Herkenhoff, K. E., Heydari, E., Kah, L. C., Lemmon, M. T., Minitti, M. E., Olson, T. S., Parker, T. J., Rowland, S. K., Schieber, J., Sullivan, R. J., ... Goetz, W. (2012). Curiosity's Mars Hand Lens Imager (MAHLI) Investigation. *Space Science Reviews*, 170(1–4), 259–317. <https://doi.org/10.1007/s11214-012-9910-4>

Eshelman, E., Daly, M.G., Slater, G., Dietrich, P. and Gravel, J.F. (2014). An ultraviolet Raman wavelength for the in-situ analysis of organic compounds relevant to astrobiology. *Planetary and Space Science*, 93, 65-70.

Farley, K. A., Williford, K. H., Stack, K. M., Bhartia, R., Chen, A., de la Torre, M., Hand, K., Goreva, Y., Herd, C. D. K., Hueso, R., Liu, Y., Maki, J. N., Martinez, G., Moeller, R. C., Nelessen, A., Newman, C. E., Nunes, D., Ponce, A., Spanovich, N., ... Wiens, R. C. (2020). Mars 2020 Mission Overview. *Space Science Reviews*, 216(8), 142. <https://doi.org/10.1007/s11214-020-00762-y>

Farley, K. A., Stack, K., M., Horgan, B. H. N., Tarnas, J., Sun, V. Z., Shuster, D. L., et al. (2022). Aqueously altered igneous rocks on the floor of Jezero crater, Mars. *Science*, <https://doi.org/10.1126/science.abo2196>

Fernández-Remolar, D. C., Chong-Díaz, G., Ruíz-Bermejo, M., Harir, M., Schmitt-Kopplin, P., Tziotis, D., Gómez-Ortíz, D., García-Villadangos, M., Martín-Redondo, M. P., Gómez, F., Rodríguez-Manfredi, J. A., Moreno-Paz, M., De Diego-Castilla, G., Echeverría, A., Urtuvia, V. N., Blanco, Y., Rivas, L., Izawa, M. R. M., Banerjee, N. R., ... Parro, V. (2013). Molecular preservation in halite- and perchlorate-rich hypersaline subsurface deposits in the Salar Grande basin (Atacama Desert, Chile): Implications for the search for molecular biomarkers on Mars.

*Journal of Geophysical Research: Biogeosciences*, 118(2), 922–939.

<https://doi.org/10.1002/jgrg.20059>

Fones, E. M., Colman, D. R., Kraus, E. A., Nothaft, D. B., Poudel, S., Rempfert, K. R., Spear, J. R., Templeton, A. S., & Boyd, E. S. (2019). Physiological adaptations to serpentinization in the Samail Ophiolite, Oman. *The ISME Journal*, 13(7), 1750–1762. <https://doi.org/10.1038/s41396-019-0391-2>

Fox-Powell, M. G., & Cockell, C. S. (2018). Building a Geochemical View of Microbial Salt Tolerance: Halophilic Adaptation of *Marinococcus* in a Natural Magnesium Sulfate Brine.

*Frontiers in Microbiology*, 9, 739. <https://doi.org/10.3389/fmicb.2018.00739>

Fu, X., Wang, A., & Krawczynski, M. J. (2017). Characterizing amorphous silicates in extraterrestrial materials: Polymerization effects on Raman and mid-IR spectral features of alkali and alkali earth silicate glasses: Characterizing amorphous silicates in extraterrestrial materials.

*Journal of Geophysical Research: Planets*, 122(5), 839–855.

<https://doi.org/10.1002/2016JE005241>

Fries, M. D., Lee, C., Bhartia, R., Razzell Hollis, J., Beegle, L. W., Uckert, K., Graff, T. G., Abbey, W., Bailey, Z., Berger, E. L., Burton, A. S., Callaway, M. J., Cardarelli, E. L., Davis, K. N., DeFlores, L., Edgett, K. S., Fox, A. C., Garrison, D. H., Haney, N. C., ... Aileen Yingst, R.

(2022). The SHERLOC Calibration Target on the Mars 2020 Perseverance Rover: Design, Operations, Outreach, and Future Human Exploration Functions. *Space Science Reviews*, 218(6), 46. <https://doi.org/10.1007/s11214-022-00907-1>

Garczynski, B. J., Bell, J. F., Horgan, B. H. N., Johnson, J. R., Rice M. S., Vaughan, J. I., et al. (2022). Perseverance and the purple coating: A MASTCAM-Z multispectral story (abstract). 53rd Lunar and Planetary Science Conference.

Heinz, J., Krahn, T., & Schulze-Makuch, D. (2020). A New Record for Microbial Perchlorate Tolerance: Fungal Growth in NaClO<sub>4</sub> Brines and its Implications for Putative Life on Mars. *Life*, 10(5), 53. <https://doi.org/10.3390/life10050053>

Heinz, J., Waajen, A. C., Airo, A., Alibrandi, A., Schirmack, J., & Schulze-Makuch, D. (2019). Bacterial Growth in Chloride and Perchlorate Brines: Halotolerances and Salt Stress Responses of *Planococcus halocryophilus*. *Astrobiology*, 19(11), 1377–1387. <https://doi.org/10.1089/ast.2019.2069>

Horgan B. H. N., Rice, M. S., Garczynski, B. J., Johnson J. R., Stack, K. M., Vaughan, J. I., et al. (2022). Mineralogy, morphology, and geochronological significance of the Máaz formation and the Jezero Crater Floor (abstract). 53rd Lunar and Planetary Science Conference.

Huang, E., Chen, C. H., Huang, T., Lin, E. H., Xu, J. (2000). Raman spectroscopic characteristics of Mg-Fe-Ca pyroxenes. *American Mineralogist*, 85, 3-4.

Ishibashi, H., Arakawa, M., Ohi, S., Yamamoto, J., Miyake, A., Kagi, H. (2008). Relationship between Raman spectral pattern and crystallographic orientation of a rock-forming mineral: a case study of Fo<sub>89</sub> Fa<sub>11</sub> olivine. *Journal of Raman spectroscopy*, 39(11).

Kuebler, K. E., Jolliff, B. L., Wang, A., & Haskin, L. A. (2006). Extracting olivine (Fo–Fa) compositions from Raman spectral peak positions. *Geochimica et Cosmochimica Acta*, 70(24), 6201–6222. <https://doi.org/10.1016/j.gca.2006.07.035>

Kotler, J. M., Hinman, N. W., Yan, B., Stoner, D. L., & Scott, J. R. (2008). Glycine Identification in Natural Jarosites Using Laser Desorption Fourier Transform Mass Spectrometry: Implications for the Search for Life on Mars. *Astrobiology*, 8(2), 253–266. <https://doi.org/10.1089/ast.2006.0102>

Lenz, D. D., & Ayres, T. R. (1992). Errors Associated with Fitting Gaussian Profiles to Noisy Emission-Line Spectra. *Publications of the Astronomical Society of the Pacific*, 104(681), 1104–1106.

Lieftink, D. J., Nijland, T. G., Maijer, C. (1994). The behavior of rare-earth elements in high-temperature Cl-bearing aqueous fluids; results from the Odegardens Verk natural laboratory. *The Canadian Mineralogist*, 32(1).

Litasov, K. D., & Podgornykh, N. M. (2017). Raman spectroscopy of various phosphate minerals and occurrence of tuite in the Elga IIE iron meteorite. *Journal of Raman Spectroscopy*, 48(11).

Liu, Y., Tice, M. M., Schmidt, M. E., Treiman, A. H., Kizovski, T. V., Hurowitz, J. A., et al. (2022). An olivine cumulate outcrop on the floor of Jezero crater, Mars. *Science*, <https://doi.org/10.1126/science.abo2756>

Mason, H. E., McCubbin, F. M., Smirnov, A., and Phillips, B. L. (2009). Solid-state NMR and IR spectroscopic investigation of the role of structural water and F in carbonate-rich fluorapatite. *American Mineralogist*, 94(4).

McCubbin, F. M., Hauri, E. H., Elardo, S. M., Vander Kaaden, K. E., Wang, J., Shearer Jr, C. K. (2012), Hydrous melting of the Martian mantle produced both depleted and enriched shergottites. *Geology*, 40(8).

McCubbin, F. M., Phillips, B. L., Adcock, C. T., Tait, K. T., Steele, A., Vaughn, J. S., Fries, M.D., Atudorei, V., Vander Kaaden, K. E., and Hausrath, E. M. (2018). Discreditation of bobdownsite and the establishment of criteria for the identification of minerals with essential monofluorophosphate ( $\text{PO}_3\text{F}^{2-}$ ). *American Mineralogist: Journal of Earth and Planetary Materials*, 103(8).

McNaught, A. D., Wilkinson, A. (1997). Compendium of chemical terminology. Blackwell Science.

Meslin, P.-Y., Forni, O., Beck, P., Cousin, A., Beyssac, O., Lopez-Reyes, G., et al.. (2022). Evidence for perchlorate and sulfate salts in Jezero Crater, Mars, from SuperCam observations (abstract). 53rd Lunar and Planetary Science Conference.

Moeller, R. C., Jandura, L., Rosette, K., Robinson, M., Samuels, J., Silverman, M., et al. (2021). The Sampling and Caching Subsystem (SCS) for the Scientific Exploration of Jezero Crater by the Mars 2020 Perseverance Rover. *Space Science Reviews*, 217(1), 5.  
<https://doi.org/10.1007/s11214-020-00783-7>

Montagnac, G., Hao, J., Pedreira-Segade, U., & Daniel, I. (2021). Detection of nucleotides adsorbed onto clay by UV resonant Raman spectroscopy: A step towards the search for biosignatures on Mars. *Applied Clay Science*, 200, 105824.  
<https://doi.org/10.1016/j.clay.2020.105824>

Morris, R. V., Haney, N. C., Jakubek, R. S., Fries, M. D., Clark, J. V., Lee, L., and Mertzman, S. A. (2022). Relative detectability of iron-bearing phases for the Mars 2020 SHERLOC deep UV Raman instrument: 1. Focusing on carbonates (abstract). 53rd Lunar and Planetary Science Conference.

Núñez, J. I., Johnson J. R., Horgan B. H. N., Rice M. S., Vaughan A., Tate, C., et al. (2022). Stratigraphy and mineralogy of the deposits within Séítah region on the floor of Jezero Crater, Mars as seen with Mastcam-Z (abstract). 53rd Lunar and Planetary Science Conference.

O'shea, D. C., Bartlett, M. L., Young, R. A. (1974). Compositional analysis of apatites with laser-Raman spectroscopy: (OH, F, Cl) apatites. *Archives of Oral Biology*, 19(11).

Razzell Hollis, J., Abbey, W., Beegle, L. W., Bhartia, R., Ehlmann, B. L., Miura, J., Monacelli, B., Moore, K., Nordman, A., Scheller, E., Uckert, K., & Wu, Y.-H. (2021a). A deep-ultraviolet Raman and Fluorescence spectral library of 62 minerals for the SHERLOC instrument onboard

Mars 2020. *Planetary and Space Science*, 209, 105356.

<https://doi.org/10.1016/j.pss.2021.105356>

Razzell Hollis, J., Ireland, S., Abbey, W., Bhartia, R., & Beegle, L. W. (2021b). Deep-ultraviolet Raman spectra of Mars-relevant evaporite minerals under 248.6 nm excitation. *Icarus*, 357, 114067. <https://doi.org/10.1016/j.icarus.2020.114067>

Razzell Hollis, J., Moore, K. R., Sharma, S., Beegle, L., Grotzinger, J. P., Allwood, A., et al., (2022). The power of paired proximity science observations: Co-located data from SHERLOC and PIXL on Mars. *Icarus*, 387(15). <https://doi.org/10.1016/j.icarus.2022.115179>

Scheller, E.L., Razzell Hollis, J., Cardarelli, E. L., Steele, A., Beegle, L. W., Bhartia, R., et al. (2022). Aqueous alteration processes and implications for organic geochemistry in Jezero crater, Mars. *Science*, 378(6624). <https://doi.org/10.1126/science.abo5204>

Schmidt, M. E., Allwood A., Christian, J., Clark, B. C., Flannery, D., Hennecke, J., et al. (2022). Highly differentiated basaltic lavas examined by PIXL in Jezero Crater (abstract). 53rd Lunar and Planetary Science Conference.

Schopf, J. W., Farmer, J. D., Foster, I. S., Kudryavtsev, A. B., Gallardo, V. A., & Espinoza, C. (2012). Gypsum-Permineralized Microfossils and Their Relevance to the Search for Life on Mars. *Astrobiology*, 12(7), 619–633. <https://doi.org/10.1089/ast.2012.0827>

Shkolyar, S., & Farmer, J. D. (2018). Biosignature Preservation Potential in Playa Evaporites: Impacts of Diagenesis and Implications for Mars Exploration. *Astrobiology*, 18(11), 1460–1478. <https://doi.org/10.1089/ast.2018.1849>

Shkolyar, S., Lalla, E., Konstantinidis, M., Cote, K., Daly, M. G., & Steele, A. (2021). Detecting Ce<sup>3+</sup> as a biosignature mimicker using UV time-resolved laser-induced fluorescence and Raman spectroscopy: Implications for planetary missions. *Icarus*, 354, 114093. <https://doi.org/10.1016/j.icarus.2020.114093>



Simon, J. I., Amundsen, H. E. F., Beegle, L. W., Bell J., Benison, K. C., Berger., E. L., et al. (2022). Sampling of Jezero Crater Máaz Formation by Mars 2020 Perseverance rover (abstract). 53rd Lunar and Planetary Science Conference.

Stack, K. M., et al. (2020). Photogeologic Map of the Perseverance Rover Field Site in Jezero Crater Constructed by the Mars 2020 Science Team. *Space Science Reviews*, 216(8), 127.

<https://doi.org/10.1007/s11214-020-00739-x>

Sudarsanan, K. T., & Young, R. A. (1969) Significant precision in crystal structural details. Holly Springs hydroxyapatite. *Acta Crystallographica Section B*, 25(8).

Sun, V. Z., Hand, K. P., Stack, K. M., Farley, K. A., Milkovich, S., Kronyak, R., et al. (2022). Exploring the Jezero Crater floor: Overview of results from the Mars 2020 Perseverance Rover's first science campaign (abstract). 53rd Lunar and Planetary Science Conference.

Tarcea, N., Harz, M., Rösch, P., Frosch, T., Schmitt, M., Thiele, H., Hochleitner, R., & Popp, J. (2007). UV Raman spectroscopy—A technique for biological and mineralogical in situ planetary studies. *Spectrochimica Acta Part A: Molecular and Biomolecular Spectroscopy*, 68(4), 1029–1035. <https://doi.org/10.1016/j.saa.2007.06.051>

Twing, K. I., Brazelton, W. J., Kubo, M. D. Y., Hyer, A. J., Cardace, D., Hoehler, T. M., McCollom, T. M., & Schrenk, M. O. (2017). Serpentinization-Influenced Groundwater Harbors Extremely Low Diversity Microbial Communities Adapted to High pH. *Frontiers in Microbiology*, 8. <https://doi.org/10.3389/fmicb.2017.00308>

Uckert, K., Bhartia, R., Beegle, L. W., Monacelli, B., Asher, S. A., Burton, A. S., Bykov, S. V., Davis, K., Fries, M. D., Jakubek, R. S., Hollis, J. R., Roppel, R. D., & Wu, Y.-H. (2021).

Calibration of the SHERLOC Deep Ultraviolet Fluorescence–Raman Spectrometer on the Perseverance Rover. *Applied Spectroscopy*, 75(7), 763–773.

<https://doi.org/10.1177/00037028211013368>

Udry, A., Sautter, V., Cousin, A., Wiens, R. C., Forni, O., Benzerara, K., et al. (2022). A Mars 2020 Perseverance SuperCam perspective on the igneous nature of the Máaz formation at Jezero crater, Mars (abstract). 53rd Lunar and Planetary Science Conference.

Walrafen, G. E., Krishnan, P. N. (1981). Raman spectrum of pressure compacted fused silica. *The Journal of Chemical Physics*, 74(9).

Wang, A., Freeman, J. J., Jolliff, B. L., & Chou, I.-M. (2006). Sulfates on Mars: A systematic Raman spectroscopic study of hydration states of magnesium sulfates. *Geochimica et Cosmochimica Acta*, 70(24), 6118–6135. <https://doi.org/10.1016/j.gca.2006.05.022>

Wiens, R. C., Udry, A., Mangold, N., Beyssac, O., Quantin, C., Sautter, V., et al. (2022). Composition and density stratification observed by SuperCam in the first 300 sols in Jezero Crater (abstract). 53rd Lunar and Planetary Science Conference.

Wogoland, B. V., Minitti, M. E., Kah, L. C., Yingst, R. A., Hickman-Lewis, K., Sharma, S., et al., (this issue). Science and Science-Enabling Activities of the SHERLOC and WATSON Imaging Systems in Jezero Crater, Mars. *JGR:Planets*

Wojdyr, M. (2010). Fityk: A general-purpose peak fitting program. *Journal of Applied Crystallography*, 43(5), 1126–1128. <https://doi.org/10.1107/S0021889810030499>

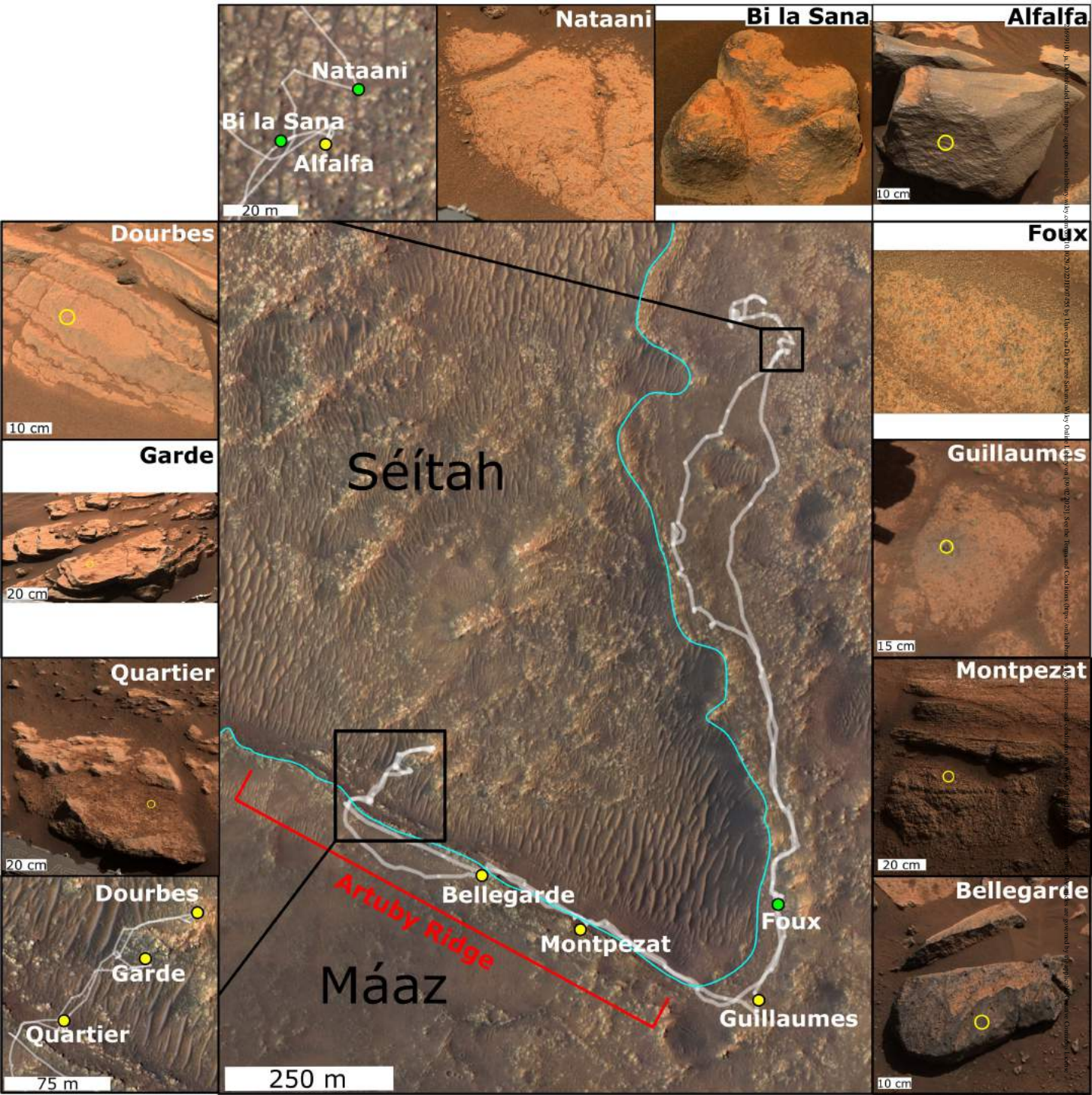
Woycheese, K. M., Meyer-Dombard, D. R., Cardace, D., Argayosa, A. M., & Arcilla, C. A. (2015). Out of the dark: Transitional subsurface-to-surface microbial diversity in a terrestrial serpentinizing seep (Manleluag, Pangasinan, the Philippines). *Frontiers in Microbiology*, 6. <https://doi.org/10.3389/fmicb.2015.00044>

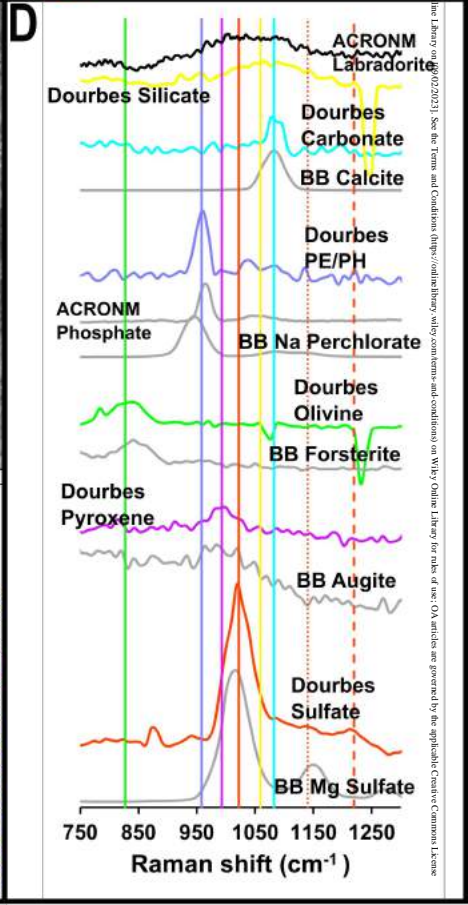
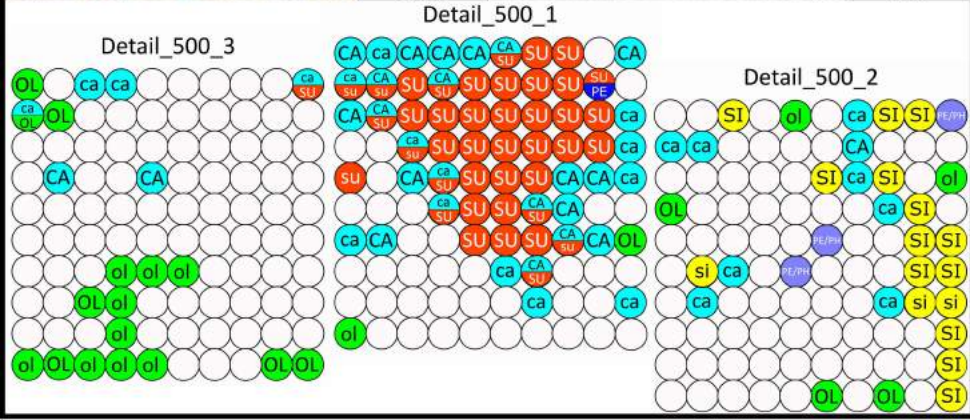
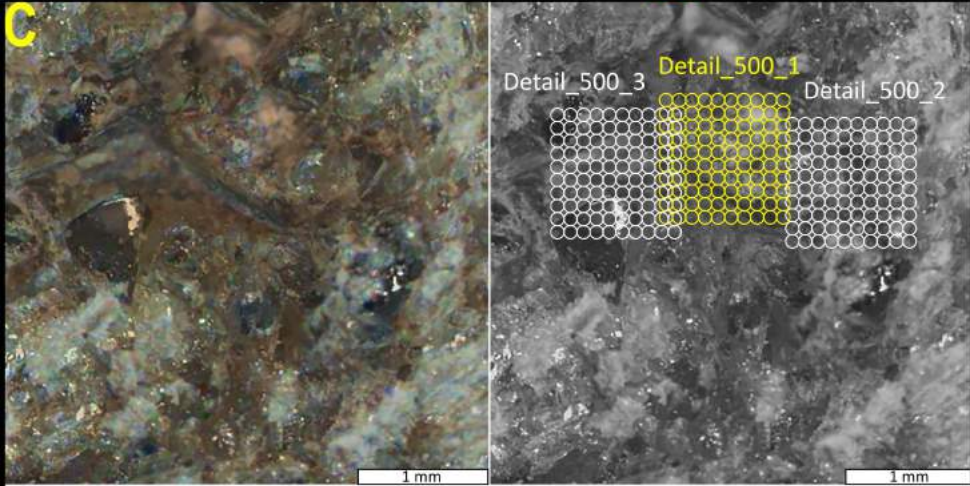
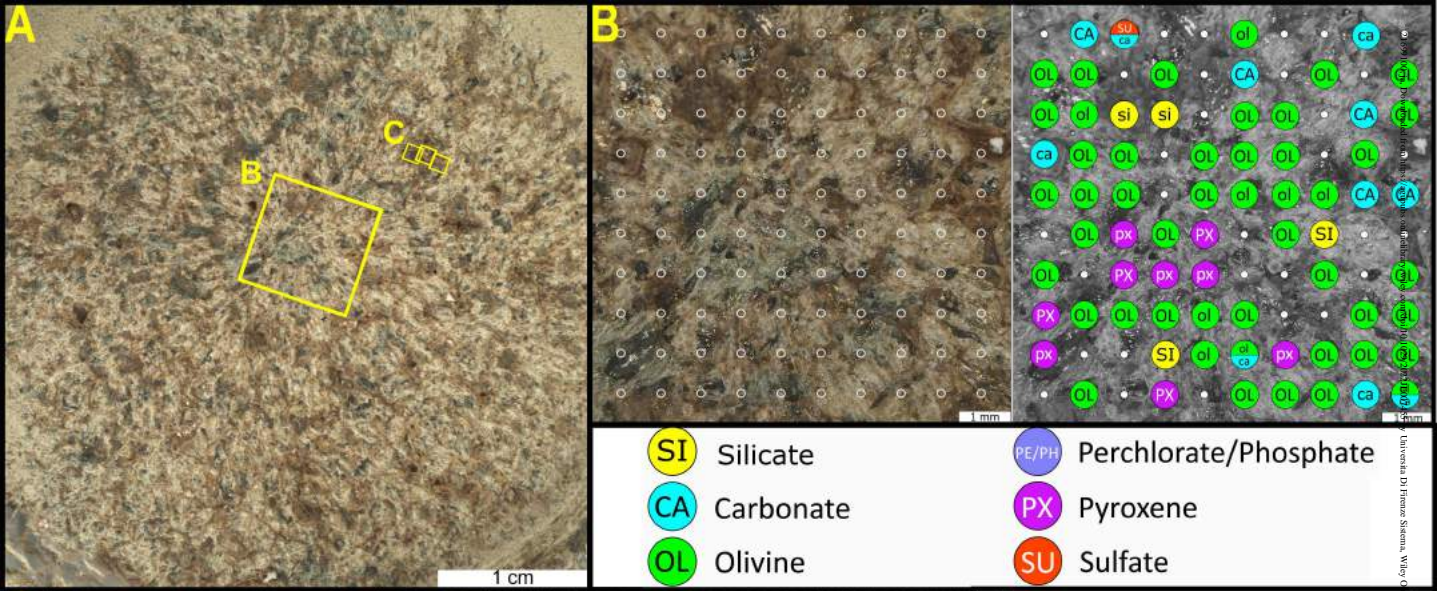
Xing, T., Zhu, W., Fuisseis, F., & Lisabeth, H. (2018). Generating porosity during olivine carbonation via dissolution channels and expansion cracks. *Solid Earth*, 9(4), 879–896.

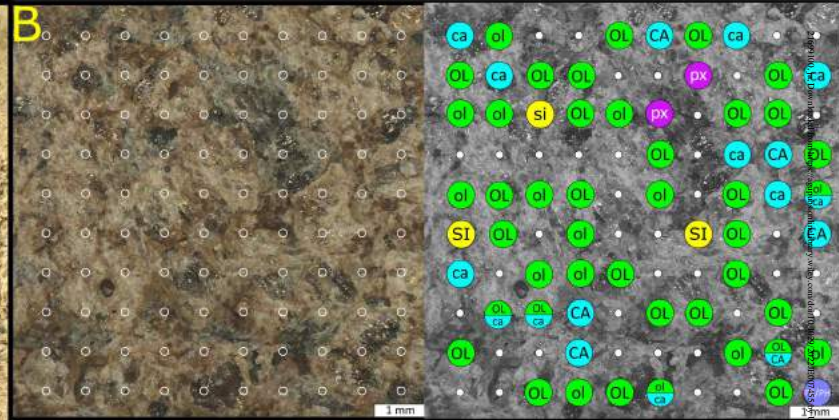
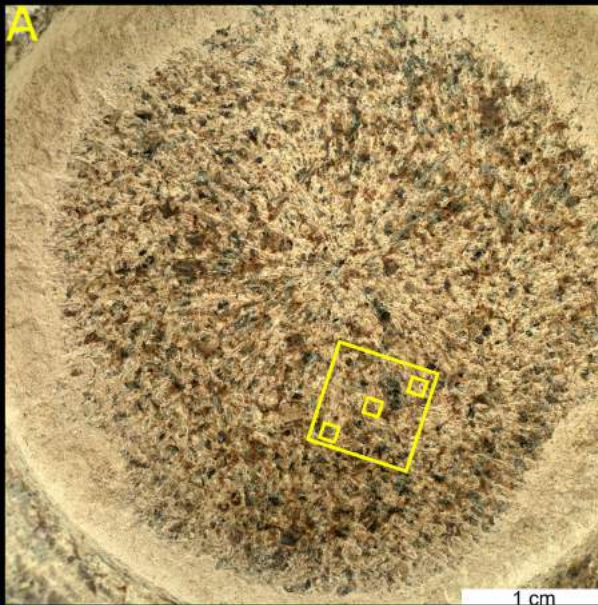
<https://doi.org/10.5194/se-9-879-2018>

Zapata, F., Garcia-Ruiz, C. (2018). The discrimination of 72 nitrate, chlorate and perchlorate salts using IR and Raman spectroscopy. *Spectrochimica Acta A*, 189.

Accepted Article







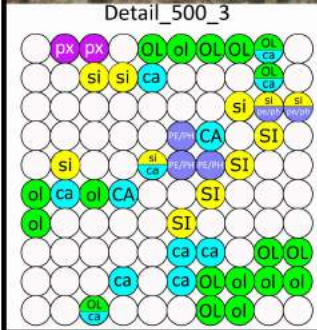
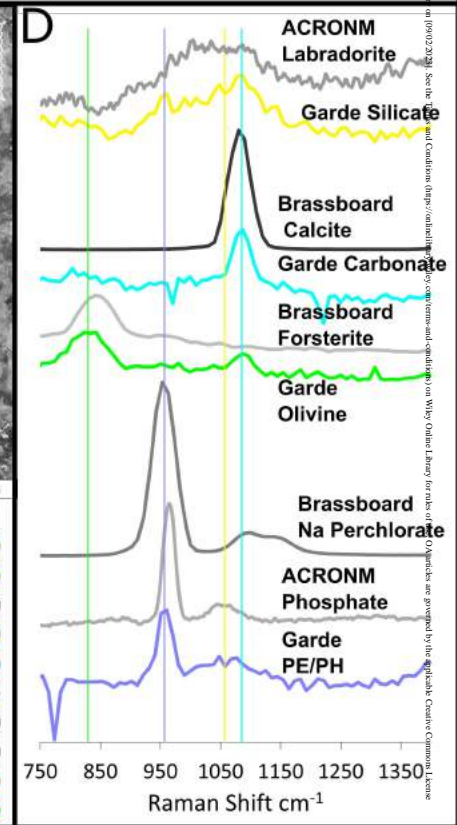
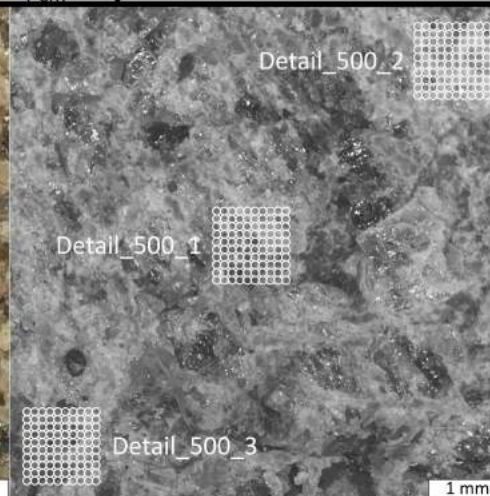
**SI** Silicate

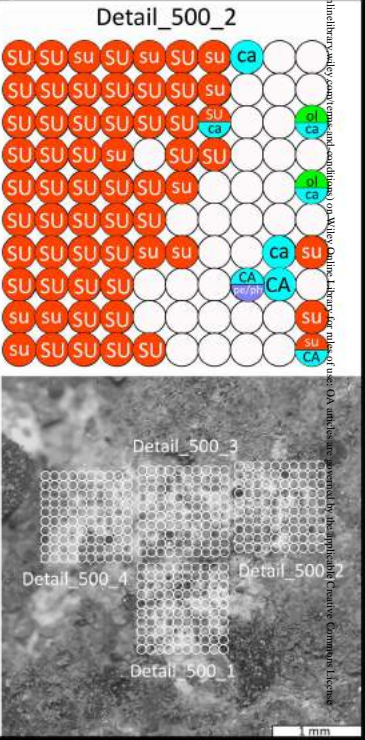
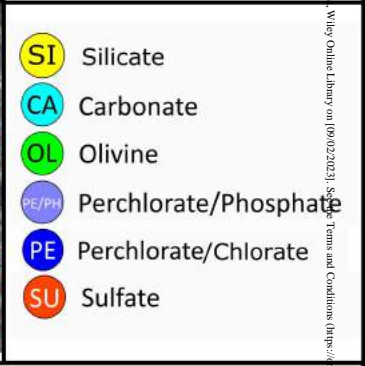
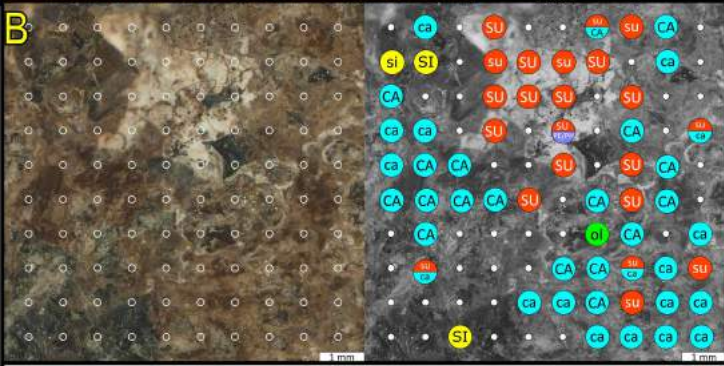
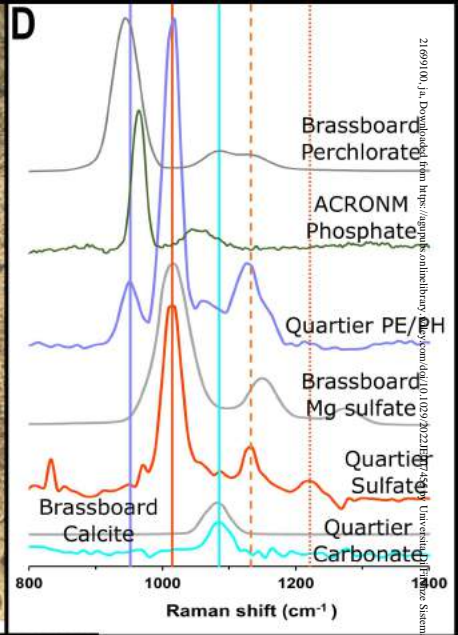
**CA** Carbonate

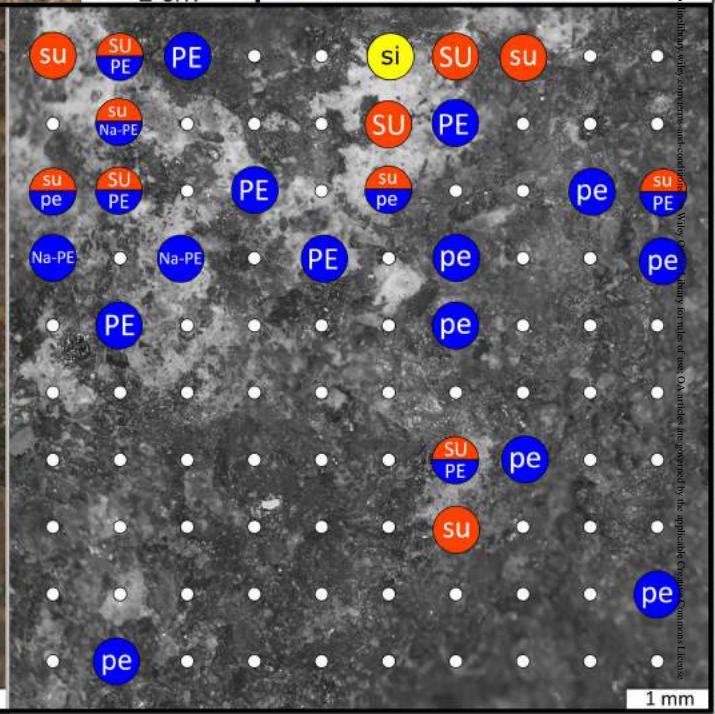
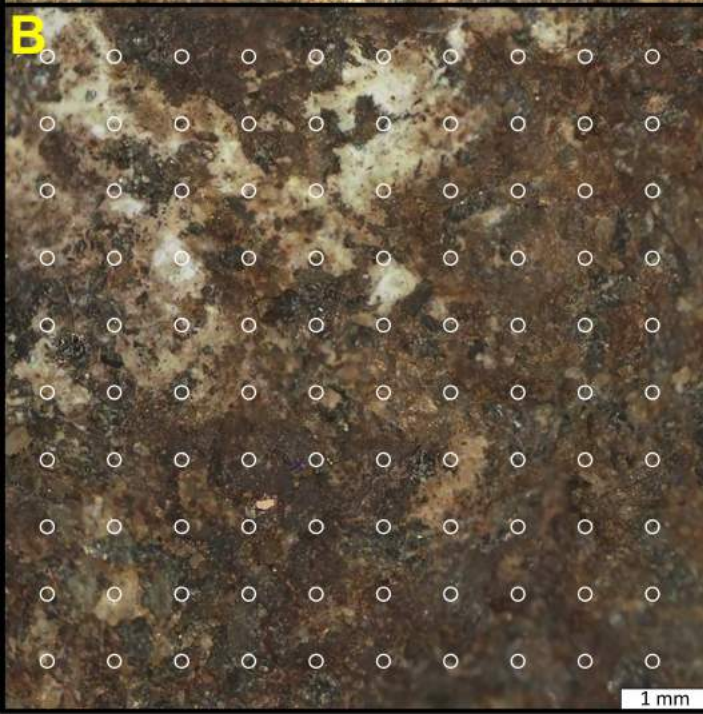
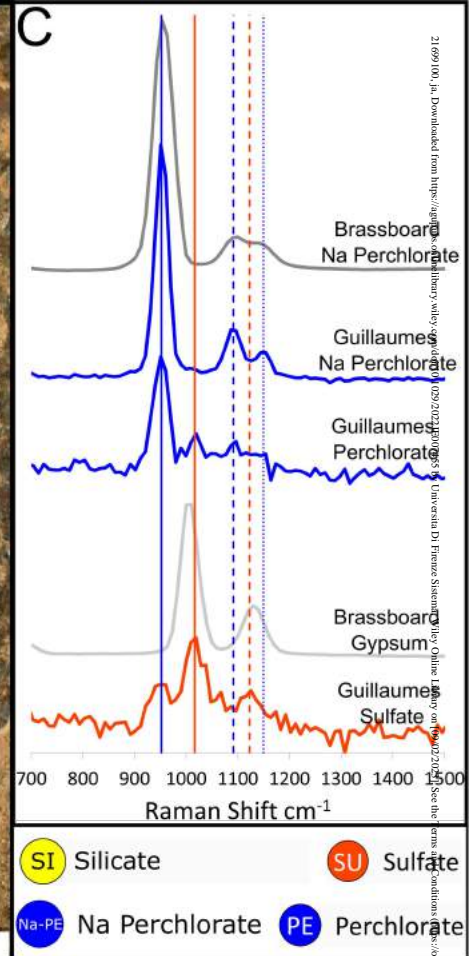
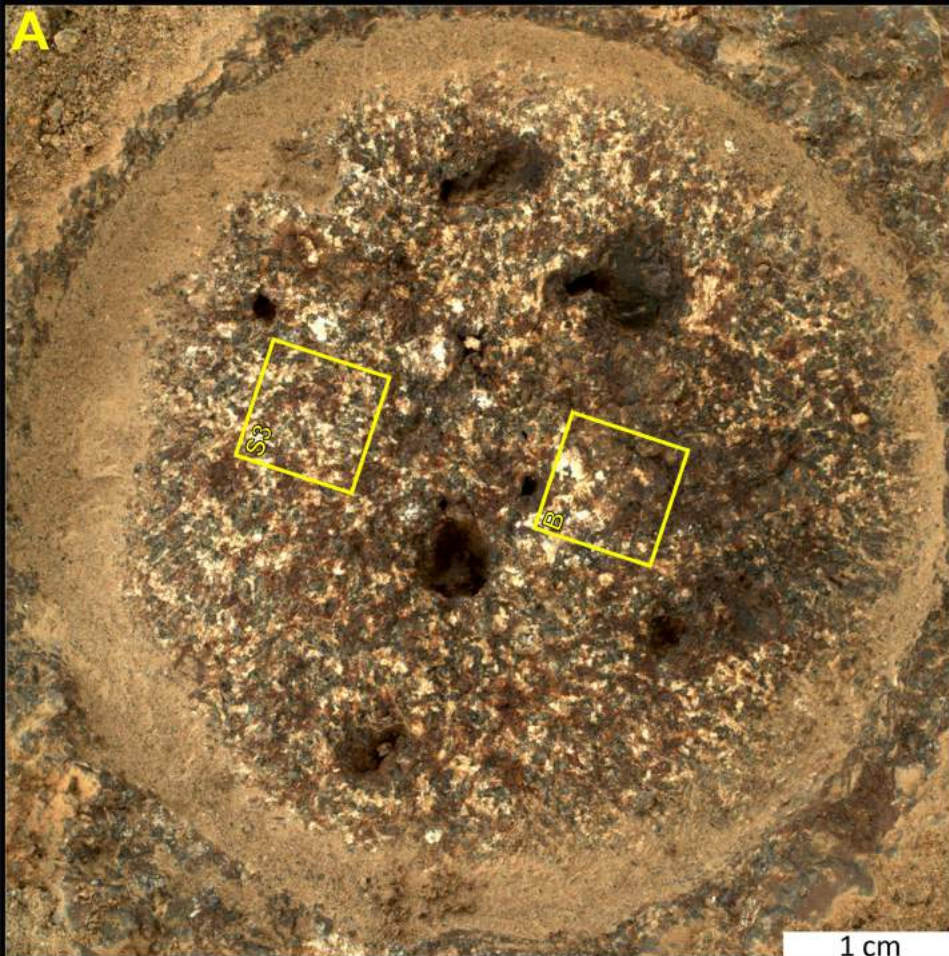
**OL** Olivine

**PX** Pyroxene

**PE/PH** Perchlorate/Phosphate



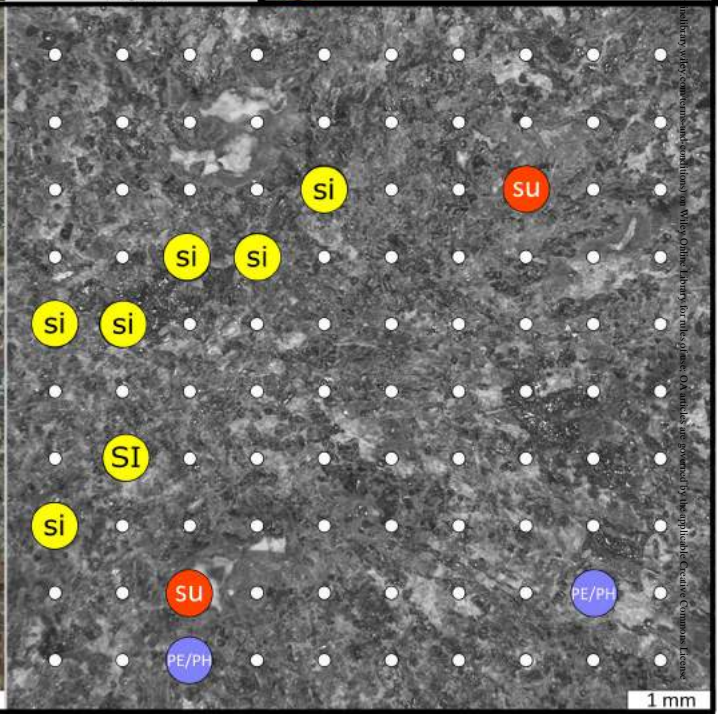
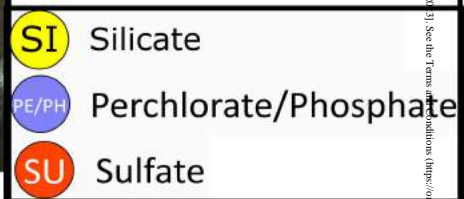
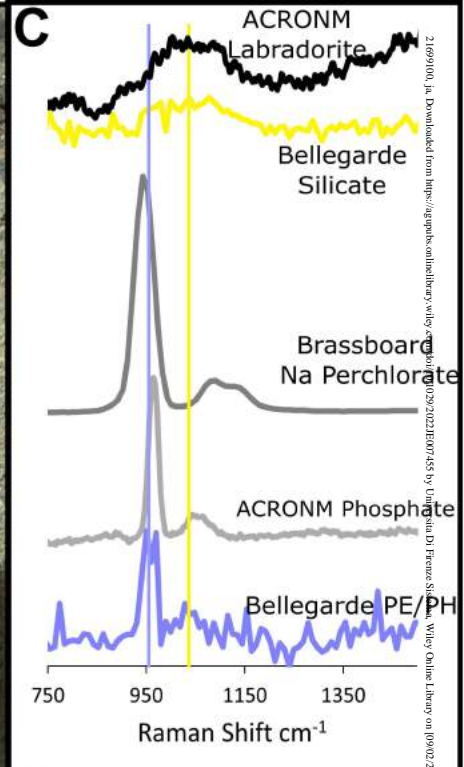




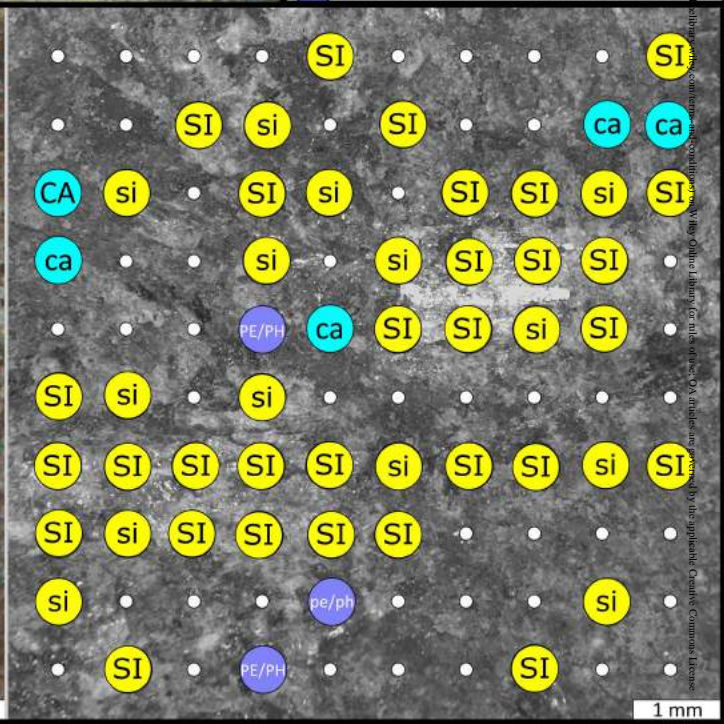
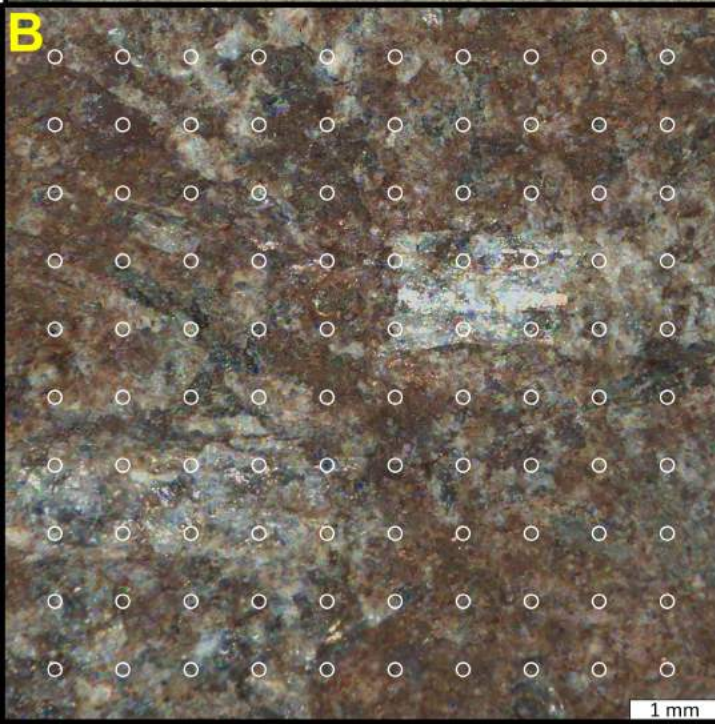
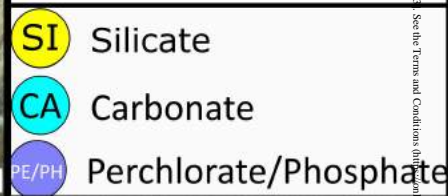
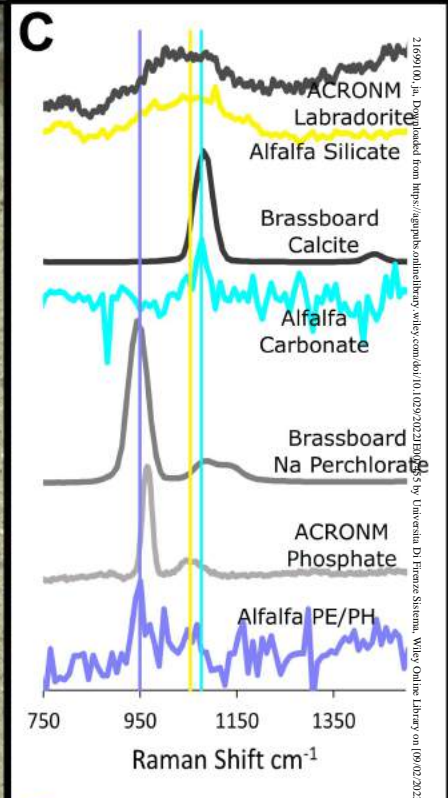
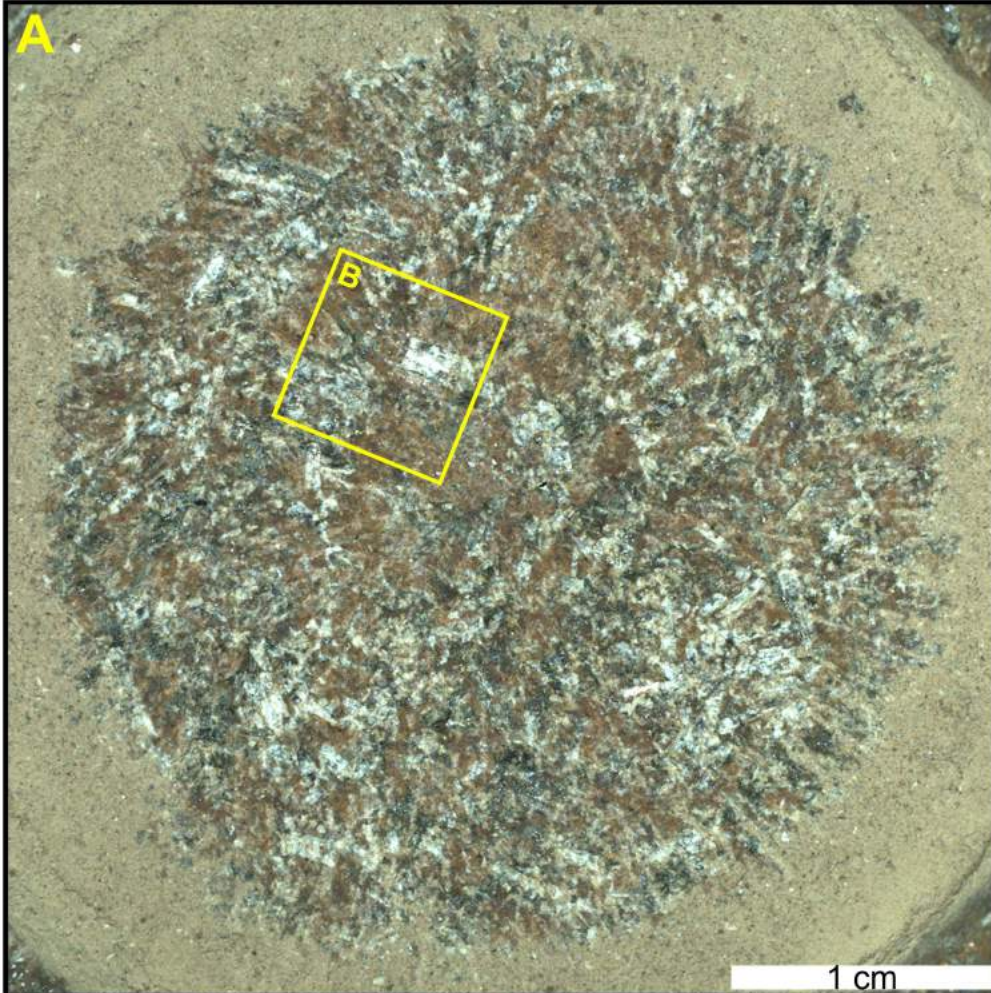
21699-100, JPL Downloaded from https://pubs.aip.org/jpl/article-pdf/10/2/21699-100/14930000 by Universita Di Firenze Sierreni on 04/11/2019. See the Terms and Conditions (https://pubs.aip.org/termsandconditions) on AIP.org for rules of use; OA articles are governed by the applicable Creative Commons License







21699100, *J. Downloaded from https://pubs.onlinelibrary.wiley.com/doi/10.1002/2022JHE07458 by Universita Di Firenze S.p.A., Wiley Online Library on [09/02/2023]. See the Terms and Conditions (https://onlinelibrary.wiley.com/terms-and-conditions) on Wiley Online Library for rules of use; OA articles are governed by the applicable Creative Commons License*



21691001, J. Downloaded from https://academic.oup.com/ps/advance-article-abstract/doi/10.1093/ps/psab015/6311111 by Universita Di Firenze System, Wiley Online Library on [09/02/2022]. See the Terms and Conditions (https://onlinelibrary.wiley.com/terms-and-conditions) on Wiley Online Library for rules of use; OA articles are governed by the applicable Creative Commons License

# Abraded Target Mineral Detections

